Modeling Nonconfined Density Currents Using 3D Hydrodynamic Models

B. Pérez-Díaz[1]; S. Castanedo[2]; P. Palomar[3]; F. Henno[4]; and M. Wood[5]

Abstract: Density currents generated by marine brine discharges, e.g., from desalination plants, can have a negative impact on marine ecosystems. It is therefore important to accurately predict their behavior. Predictions are often made using computational hydrodynamic models, which should be validated using field or laboratory measurements. This paper focuses on the setup and validation of three-dimensional (3D) models for estimating the transport and mixing processes that occur in these types of flows. Through a comprehensive sensitivity analysis based on the reproduction of several laboratory-generated density currents, a set of recommendations are made regarding the modeling aspects, including the domain discretization, the treatment of momentum at the density current source, the hydrostatic hypothesis and the selection of turbulence closure models. Finally, the proposed numerical model setup is validated using different experimental data showing good agreement in terms of the main variables considered: errors of less than 1.3% for dilution and of 6% for velocity. This study serves as a first step toward the full validation of these 3D hydrodynamic models for the simulation of field-scale density currents.
DOI: 10.1061/(ASCE)HY.1943-7900.0001563.

Introduction

Bottom density-driven flows, which are generally referred to as density or gravity currents, are continuous underflows that travel downslope due to their negatively buoyant characteristics, i.e., because they are heavier than the surrounding fluid. This phenomenon occurs widely in natural environments and is caused by either human activities or natural processes (Simpson 1997; Huppert 2006). Currently, in coastal and marine environments, some of the most common density currents are those generated by brine discharge from desalination plants. Hodges et al. (2011) make an analogy between the behavior of a natural salt wedge and such brine discharges into shallow waters, both of which are governed by the density difference, by the hydrodynamics of the surrounding area (Shao et al. 2008), and by the bottom slope. Due to the potentially negative impacts of these human-induced currents on the environment (Lattemann and Höpner 2008; Sánchez-Lizaso et al. 2008; Laspidou et al. 2010; Dawoud and Al Mulla 2012) there is a growing interest in obtaining accurate predictions of their behavior.

Dense underflows have been widely investigated in laboratory experiments (Alavian 1986; Garcia 1993; Gerber et al. 2011; Ottolenghi et al. 2017b) and field studies (Hebbert et al. 1979; Dallimore et al. 2001; Fernandez and Imberger 2006; Hodges et al. 2011). Major efforts have also been made to predict the behavior of these currents from different modeling techniques and through comparisons with previous laboratory experiments (Choi 1999; La Rocca et al. 2008; Lombardi et al. 2015; Sciortino et al. 2018). As a broad classification, two modeling techniques are available for studying these flows numerically using the hydrodynamic equations (i.e., continuity, momentum, and transport equations): integral models and those that determine the vertical structure of the flow. The integral model for density currents was first introduced by Ellison and Turner (1959) and was further developed by Alavian (1986) and Parker et al. (1986) among others, primarily focused on turbidity currents (Akiyama and Stefan 1985; Parker et al. 1986; Garcia 1993; Choi and Garcia 1995; Bradford et al. 1997; Imran et al. 1998; Choi 1999). In general, these integral models assume a hydrostatic pressure distribution within the density current and use vertical depth-integrated equations. They have been designated single- or double-layer shallow water models depending on whether they consider only the heavier layer (e.g., Ungarish 2007a, b; La Rocca et al. 2008; Lombardi et al. 2018) or divide the entire depth into two layers (e.g., Ungarish 2008; La Rocca and Pinzon 2010; La Rocca et al. 2012). Note that although it has been demonstrated that these integral models are capable of providing good results under laboratory controlled conditions, they are not capable of taking into account the complexity of real environmental conditions that may occur in nature and may affect the evolution of the density current flow.

Conversely, there are numerical studies that have used models based on the resolution of three-dimensional (3D) Navier-Stokes (N-S) equations with differing degrees of simplification to solve the vertical structure of density current flows. Specifically, the vertical distribution of the main variables of density currents has been numerically analyzed from hydrodynamic models that solve N-S equations taking into account the Reynolds approximation (Reynolds-averaged Navier-Stokes equations or RANS). In these applications, a turbulence closure model (TCM) estimates the Reynolds stress in conjunction with wall functions. Stacey and Bowen (1988a, b) solved the vertical distribution of one-dimensional turbidity currents using a mixing length model as the TCM. Other authors have employed the κ-ε model (Rodi 1984) as

[1]Environmental Hydraulics Institute "IH Cantabria," Universidad de Cantabria, 39011 Santander, Spain (corresponding author). ORCID: https://orcid.org/0000-0002-1987-2605. Email: perezdb@unican.es

[2]Departamento de Ciencias y Técnicas del Agua y del Medio Ambiente, Universidad de Cantabria, 39005 Santander, Spain. Email: castanedos@unican.es

[3]Ministry of Agriculture, Food and Environment, 28071 Madrid, Spain. Email: palomarpilar@yahoo.es

[4]Coasts and Oceans Group, HR Wallingford, Oxfordshire OX10 8BA, UK. Email: f.henno@hrwallingford.com

[5]Coasts and Oceans Group, HR Wallingford, Oxfordshire OX10 8BA, UK. Email: m.wood@hrwallingford.com

Note. This manuscript was submitted on February 20, 2018; approved on August 1, 2018No Epub Date. Discussion period open until 0, 0; separate discussions must be submitted for individual papers. This paper is part of the ***Journal of Hydraulic Engineering***, © ASCE, ISSN 0733-9429.

the TCM (e.g., Eidsvik and Brørs 1989; Brørs and Eidsvik 1992; Choi and Garcia 2002). The κ-ε model has also been applied to density currents plunging into reservoirs by Farrell and Stefan (1988) and Bournet et al. (1999). In recent years, a number of direct numerical simulations (DNSs) of density currents have been reported in the literature (e.g., Härtel et al. 2000; Lowe et al. 2005; Birman et al. 2005; Cantero et al. 2006, 2007). These more sophisticated simulations are capable of capturing interfacial vortex dynamics such as Kelvin-Helmholtz instabilities and the formation of lobe-cleft structures at the current head. Other authors such as Patterson et al. (2005, 2006) have conducted simulations of axisymmetric density currents using implicit large eddy simulations (LESs) (Almgren et al. 1996) relying on the use of subgrid scale modeling (SGS). Nowadays, there are several remarkable studies focused on LESs of different kinds of density currents (e.g., Ottolenghi et al. 2016a, b, 2017a, 2018). However, DNS and LES are still prohibitively expensive in terms of computational time and especially when considering field-scale simulations.

An alternative to these models based on the resolution of the hydrodynamic equations is given by the lattice Boltzmann method (LBM), defined in the framework of the kinetic theory, which describes the flow in terms of probability density functions. The simplicity and versatility of the LBM has encouraged its development in the computations fluids dynamics within the last decade (e.g., Aidun and Clausen 2010). Regarding the reproduction of complex flows such as density currents, Rocca et al. (2012) developed a LBM for two-layered shallow-water flows by considering two separate sets of LBM equations, one for each layer, obtaining good agreement between the LBM numerical results and the experimental results when the evolution of the flow does not depend on the viscosity. Recently, Ottolenghi et al. (2018) revels that this alternative can be also applied for three-dimensional numerical simulations of density currents for different Reynolds number by implementing an equivalent large eddy simulation model in the LBM framework. Nevertheless, although LBM has been successfully applied to simulate density currents generated by laboratory experiments, both considering regular and complex geometries (e.g., Prestininzi et al. 2016), significant research still needs to be done to strengthen the LBM for simulating real field-scale density currents.

Focusing on the most developed hydrodynamic equations-based models mentioned and their application, integral models can be considered adequate for field-scale practical studies of water resources management where a coarse approximation of the characteristic flow quantities at an equilibrium state may be sufficient. Conversely, the most complex numerical approximations (e.g., DNS and LES) are highly time-demanding computationally and are typically applied at the laboratory scale under controlled conditions. However, intermediate complexity 3D hydrodynamic models can be used to solve field-scale applications; as an example, Bombardelli and Garca (2002) assessed the potential development of density currents in the Chicago River while capturing their spatial variability. Kulis and Hodges (2006) carried out a layer-number sensitivity test to numerically simulate density currents of the Corpus Christi Bay in Texas using a sigma-coordinate 3D hydrodynamic model based on RANS equations and while taking into account the Boussinesq approximation and the hydrostatic hypothesis. Applying similar 3D hydrodynamic models, Firoozabadi et al. (2009) and Mahgoub et al. (2015) simulated density currents and validated their results against some laboratory measurements. Nevertheless, to the authors' knowledge, none of the reviewed studies have been fully validated, i.e., considering both horizontal spreading and the vertical structure of the main flow variables (velocity and concentration). In addition, none of these studies provide recommendations to accurately reproduce these kind of flows. This will be very useful in practical purposes such as the design of brine discharges into seawater, which have to meet strict water quality criteria regarding the salinity concentration far from the discharge point (e.g., Sánchez-Lizaso et al. 2008).

The current paper focuses on establishing a suitable setup of a 3D hydrodynamic model based on RANS equations, while taking into account the Boussinesq approximation and the hydrostatic or nonhydrostatic pressure hypothesis, for simulating nonconfined density currents. The study numerically reproduces a set of laboratory experiments carried out in the Environmental Hydraulics Institute (IHCantabria) by applying advanced optical techniques (Pérez-Díaz et al. 2016, 2018), as well as reproducing other experiments under different flow conditions presented by Choi and Garcia (2001). The numerical simulations are fully calibrated and validated against laboratory measurements by comparing the main flow and mixing characteristics. Therefore, the present paper outlines an optimum modeling setup that predicts the behavior of these types of flows using 3D hydrodynamic models. In addition, taking into account that these models are also capable of simulating real environmental conditions that may affect field-scale density currents (Shao et al. 2008), the findings of this study are also presented as a starting point for future field-scale studies.

The paper is presented as follows. First, the methods used are introduced, then the calibration results obtained through a comprehensive sensitivity analysis are presented and discussed. Third, the validation results are presented, and finally conclusions are drawn.

Methods

Numerical Model

The numerical model used in this study is TELEMAC-3D. Is is an open-source 3D hydrodynamic model (Hervouet 2007; LNHE 2007) that solves the three-dimensional hydrodynamic equations (i.e., continuity, momentum, and transport equations) considering the Reynolds and Boussinesq approximations. This model was adopted for this study because it combines a number of suitable characteristics to simulate these types of flows. These include a large number of subroutines based on a large volume of scientific literature that reproduces processes at different scales; a clearly structured Fortran90 source code that allows for simple user programming and modification of subroutines; the option of using both hydrostatic and nonhydrostatic pressure formulations; the variable sigma-layer coordinate (i.e., terrain-following) for vertical domain discretization; and unstructured horizontal domain discretization that allows computationally efficient high resolution results for specific areas (e.g., near sources and sinks of water, or around complex geometric features). Brief descriptions of such model features that play an important role in reproducing the behavior of density currents are listed subsequently.

Regarding turbulence modeling, TELEMAC-3D uses the eddy viscosity and diffusivity concepts (ν_t and Γ coefficients, respectively) of the Boussinesq approach. To estimate the values of these turbulence coefficients, several TCMs can be used, such as zero-equation models (based on an algebraic relation), single equation models (based on a combination of an algebraic relation and an equation), two-equation models (based on two transport-diffusion equations), and even more complex models (e.g., the Reynolds stress model). In this study, zero-equation models (including constant, Smagorinsky, Prandtl mixing length, and Nezu and Nakagawa mixing-length model) and a two-equation model (κ-ε) were used. The simplest TCM, the constant model, defines constant eddy viscosities and diffusivities according to the grid resolution and characteristic velocity of the type of flow motion studied (Madsen et al. 1988). Mixing length and Smagorinsky TCMs are based on the mixing-length concept proposed by Prandtl. While mixing-length TCMs such as the standard Prandtl model (Rodi 1984) and the Nezu and Nakagawa model (Nezu and Nakagawa 1993) are only applied as vertical TCMs, the Smagorinsky model (Smagorinsky 1963) is a subgrid turbulence model wherein mixing length is dependent on the grid and on a dimensionless coefficient according to the type of flow involved (anisotropic or isotropic flow). Finally, the most complex TCM used in this study is the two-equation κ-ε model. In this paper, eddy viscosities are evaluated by applying the following Kolmogorov-Prandtl relationship per direction:

$$\nu_t = c_\mu \frac{\kappa^2}{\varepsilon} \tag{1}$$

where κ = turbulent kinetic energy; ε = turbulent kinetic energy dissipation rate; and c_μ is an empirical constant. This TCM adds two more equations to the system, which are (in conservative form and with Einstein tensor notation)

$$\frac{\partial \kappa}{\partial t} + U_i \frac{\partial \kappa}{\partial x_i} = \frac{\partial}{\partial x_i}\left(\frac{\nu_t}{\sigma_\kappa}\frac{\partial \kappa}{\partial x_i}\right) + P - G - \varepsilon \tag{2}$$

$$\frac{\partial \varepsilon}{\partial t} + U_i \frac{\partial \varepsilon}{\partial x_i} = \frac{\partial}{\partial x_i}\left(\frac{\nu_t}{\sigma_\varepsilon}\frac{\partial \varepsilon}{\partial x_i}\right) + c_{1\varepsilon}\frac{\varepsilon}{\kappa}[P + (1 - c_{3\varepsilon})G] - c_{2\varepsilon}\frac{\varepsilon^2}{\kappa} \tag{3}$$

where production terms denoted by the shear P and buoyancy G values are estimated by

$$P = \nu_t\left(\frac{\partial U_i}{\partial x_j} + \frac{\partial U_j}{\partial x_i}\right)\frac{\partial U_i}{\partial x_j} = 2\nu_t D_{ij} D_{ij} \tag{4}$$

$$G = \beta g \frac{\nu_t}{\sigma_c}\frac{\partial T}{\partial x_i} \tag{5}$$

where indices i and j vary from 1 to 3 according to the direction involved; and β = fractional density, i.e., the volume expansion. The κ-ε model contains several empirical constants obtained from comprehensive data-fitting for a broad range of turbulent flows. Rodi (1984) compiled the following standard values:

$$\begin{aligned} &c_\mu = 0.09; \quad \sigma_\varepsilon = 1.00; \quad \sigma_\kappa = 1.30; \\ &c_{1\varepsilon} = 1.44; \quad c_{2\varepsilon} = 1.92; \quad c_{3\varepsilon} \approx 0\text{–}1 \end{aligned} \tag{6}$$

Among the empirical constants, $c_{3\varepsilon}$, which is associated with the buoyancy term G in Eq. (3), is originally established as equal to 1 for stable situations (i.e., when G is negative) and equal to 0 for unstable stratifications (Launder and Spalding 1974; Viollet 1988). However, definition of the empirical coefficients $c_{3\varepsilon}$ and c_μ is not straightforward. Discussions and numerical tests on these constants are presented in subsequent sections.

TELEMAC-3D uses several solution methods, including a semi-implicit finite-element method, to solve the full set of equations. Different procedures can be applied to each solution variable (i.e., velocities, depth, tracers, turbulent kinetic energy, and the dissipation rate). While the method of characteristics (Hervouet 2007) is generally used for the velocity calculations, more conservative and monotonic schemes are used for the depth and the tracers (LNHE 2007). In focusing on the advection scheme for tracers (in our case the salinity), the present study considers a second-order central-upwind scheme originally based on the Kurganov and Petrova (2007) scheme and adapted by Bourban (2013). For κ-ε variables, the default advection scheme established by TELEMAC-3D is the method of characteristics. However, a sensitivity test based on the advection scheme for these variables was carried out in this study. Finally, note that relative accuracies, number of iterations, and preconditionings for each variable required for the recommended iterative solver (conjugate gradient) are established in accordance with the recommendations made in the TELEMAC-3D user manual (LNHE 2007).

Experimental Databases

Two experimental databases were used to establish the validated setup of the TELEMAC-3D model for predicting the behavior of nonconfined density currents. The main and largest database was generated from a set of laboratory-generated density currents tested at IHCantabria's facilities. These laboratory experiments, presented in Pérez-Díaz et al. (2018), consisted of saline density currents that evolved over a gentle-slope (α) plastic-material base within a $3 \times 3 \times 1$ m^3 test tank filled with freshwater to simulate the receiving body (both fluids at the same temperature but with different saline concentration). The constant-flux saline effluent was discharged through a rectangular height-adjustable slot ($b_o \times h_0$) at the base [Fig. 1(b)], simulating the start of far field region of mixing that commonly forms when brine is discharged by submerged jets (Papakonstantis and Christodoulou 2010; Palomar 2014). Fig. 1(a) shows a schematic diagram of the experimental setup outlined. The main initial characteristics of this set of laboratory-generated density currents are listed in Table 1 and are outlined in Fig. 2. Note that Case C1 was selected as the reference case on which all other cases were modified by one of the initial parameters (thickness h_0, flow rate Q_0, slope α, or density difference $\rho_a - \rho_0$). This way, a comprehensive set of laboratory-generated density currents was carried out to experimentally characterize these kinds of flows under different flow-expected conditions.

To obtain high quality velocity and concentration measurements in the longitudinal profile of the density currents tested, the mentioned set of experiments used nonintrusive laser optical techniques, namely particle image velocimetry (PIV), and planar laser induced fluorescense (PLIF). The PIV technique consists of capturing the movements of small seeding particles within the flow between consecutive laser pulses that illuminate the flow, while PLIF consists of an indirect way to measure concentration based on capturing the light re-emision of a fluorescent dye once it is illuminated by the laser at determined wavelength. In the mentioned laboratory study, to capture the maximum covering area (1,400 mm), two LaVision Imager ProX 4 (CCD) cameras with a resolution of 2048×2048 pixels were located adjacently [Fig. 1(a)] with an overlapping zone. This configuration together with the appropriate selection of PIV and PLIF calibration parameters enabled the accurate measuring of concentrations and velocities. In addition, to study the lateral and front spreading [Fig. 2(b)], a set of photos were taken with a camera located at the upper part of the test tank that was able to capture the whole plan view. Further information on the experimental setup and on the advanced PIV-PLIF measurement techniques used to obtain this experimental database can be found in Pérez-Daíz et al. (2018).

The other experimental database used in this study was developed by Choi and Garcia (2001), who published the results of a set of density current experiments carried out in a $2.44 \times 3.66 \times 1.22$ m^3 tank. These experiments were chosen for this study because they generated nonconfined saline density currents with different initial conditions and because the authors provided all

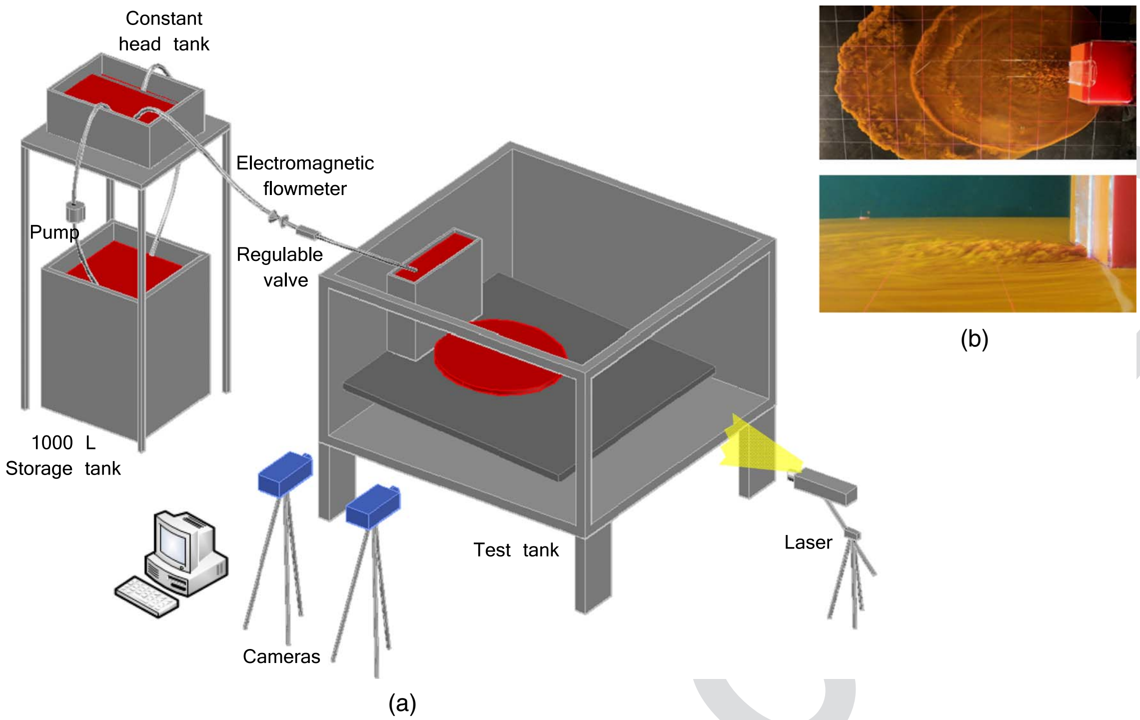

Fig. 1. (a) Schematic diagram of the PIV-LIF experimental setup; and (b) photographs of the discharge device.

Table 1. Main characteristics of laboratory configurations

Cases	Slot dimensions, $b_0 \times h_0$ (m)	Water depth, Ha_0 (m)	Slope, α (%)	Density difference, $\Delta\rho$ ($\rho_a - \rho_0$) (kg/m^3)	Discharge flow-rate, Q_0 ($u_0 b_0 h_0$) (L/min)	Buoyancy flux, Bf_0 ($Q_0 g \Delta\rho/\rho_a$) (cm^4/s^3)	Reynolds number, R_0 ($u_0 h_0/v$)	Froude$_d$ number, F_0 ($u_0/\sqrt{h_0 g_0'}$)
C1	0.1×0.026	0.46	1.0	3.14	14.60	749	2,424	3.37
C2	0.1×0.016	0.46	1.0	3.10	15.10	765	2,515	7.67
C3	0.1×0.026	0.46	1.0	3.13	19.20	984	3,197	4.47
C4	0.1×0.026	0.42	2.5	3.07	14.98	753	2,494	3.49
C5	0.1×0.026	0.36	4.5	3.14	14.09	775	2,512	3.49
C6	0.1×0.026	0.46	1.0	11.08	14.89	2,700	2,499	1.84

Source: Adapted from Pérez-Díaz et al. (2016).
Note: b_o = slot width; h_o = slot height; ρ_o = effluent density; ρ_a = ambient density; u_o = discharge velocity; g = gravity; and v = fluid viscosity.

information necessary to reproduce them numerically. Choi and Garcia (2001) studied the spreading rates of nonconfined density currents on sloping beds while varying the density difference and slope angle. The sloping bed used was composed of fiberglass, i.e., with a roughness equivalent to that of glass or Plexiglass. The initial flow parameters of these experiments are clearly detailed in Table 1 of Choi and Garcia (2001). Specifically, experiments from $DEN1$ to $DEN9$ (see Table 1 of Choi and Garcia 2001) were used in the present study.

Methodology

The present study involved of a series of more than 90 numerical simulations that reproduced the aforementioned laboratory-generated density currents. Simultaneously, data collected from the experiments were used to calibrate and validate the numerical predictions. The simulations of the calibration stage were used to create a numerical setup for predicting the behavior of these types of flows. This calibration stage consisted of a sensitivity analysis of key numerical aspects that may influence the numerical prediction of density currents such as the domain discretization, the treatment of momentum at the density current source, the hydrostatic hypothesis, and the selection of the TCM. Once the sensitivity analysis was conducted, the proposed setup was validated from a final set of simulations that reproduced the complete set of laboratory-generated density currents.

The specific methodology of the sensitivity analysis involved several simulations of the base application Case C1 (Table 1) by varying by one numerical aspect while keeping the remainder unchanged. Table 2 summarizes the numerical aspects and the variations considered in this study. The significance of the numerical aspect considered for the prediction of density current behavior was analyzed by comparing the numerical results of characteristic magnitudes such as horizontal density current spreading (b), and velocity (U) and dilution (S) evolution within the density current. Dilution was calculated using the following expression:

$$S = \frac{C_0 - C_a}{C - C_a} \tag{7}$$

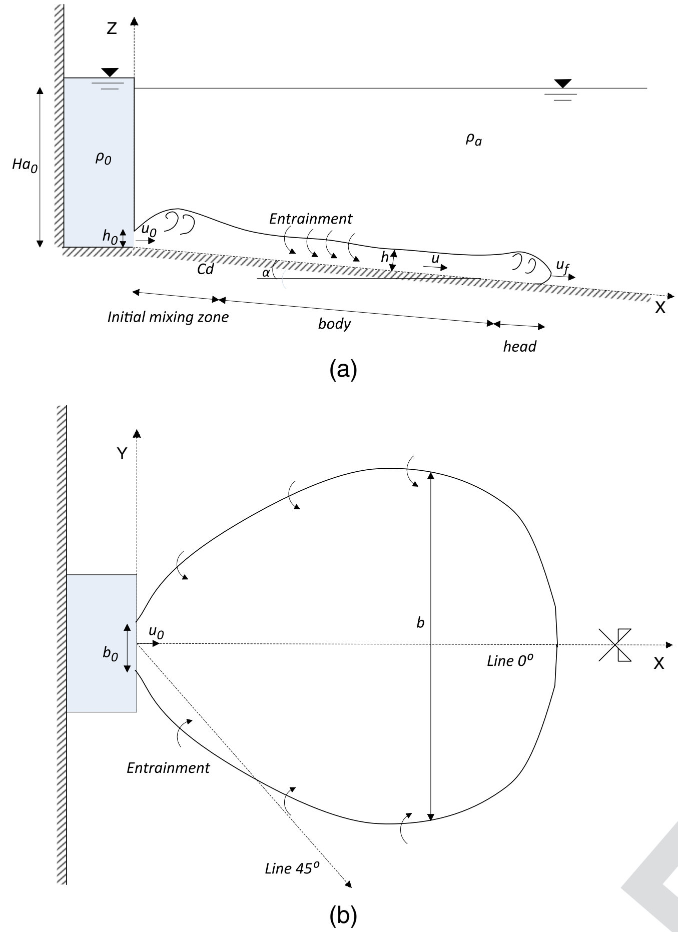

Fig. 2. Scheme of a nonconfined density current: (a) longitudinal profile view; and (b) plan view.

Table 2. Numerical aspects and their alternatives

Numerical aspect	Abbreviation	Options
Horizontal discretization	Δx	Wide range of Δx functions of b_o
Vertical discretization	Δz	Wide range of Δz functions of h_o
Source input	*Sce*	Information of Q or Q and V[a]
Hydrostatic hypothesis	*Hyd*	With or without hypothesis
Horizontal TCM	TCMh	Cst[b], Smago[c], κ-ε
Vertical TCM	TCMv	Cst, ML[d], κ-ε
Advection scheme κ-ε	$AdSch_{\kappa\varepsilon}$	Charcs[e], 2nd O-KP[f]

[a]V = injection velocity.
[b]Constant model.
[c]Smagorinsky model.
[d]Mixing-length models.
[e]Method of characteristics.
[f]Second-order Kurganov and Petrova scheme.

where C_0 = initial salinity concentration of the source; C_a = surrounding fluid salinity concentration; and C = salinity concentration at the study point within the density current.

Initial Model Setup

The initial and boundary conditions of the TELEMAC-3D applications were defined with the aim of numerically simulating the real conditions of the experimental setup. Accordingly, nodes across the domain were initialized with constant corresponding elevation values and with zero velocities (stagnant receiving water). For the boundary conditions, the free surface, open boundaries (i.e., liquid boundaries), and base and rigid walls were taken into account. At the free-surface boundary, a rigid-lid approximation that considers zero gradients and zero fluxes perpendicular to the boundary was applied (i.e., $\partial U_i/\partial z = \partial\kappa/\partial z = \partial\varepsilon/\partial z = \partial T/\partial z = 0$). At the open boundaries, streamwise gradients of all of the variables (i.e., velocities, tracer, and fluxes) were set to zero and a prescribed elevation was applied. Strictly speaking, boundary conditions for velocities subjected to rigid wall reflect a no-slip condition (i.e., Dirichlet conditions $U_i = 0$). However, due to the presence of turbulence and of a boundary layer, the velocity close to the base quickly becomes non-zero, and the no-slip condition is replaced with tangential stress [i.e., $\tau = \mu(\partial\vec{U}/\partial n)$] due to friction subjected to the base. This tangential stress is replicated by a turbulence model for the bottom using the friction or shear velocity $\tau = -\rho(U^*)^2$ and the distance to the bottom z. Assuming that the flow is hydraulically rough [i.e., the characteristic roughness size of the base is greater than the thickness of the viscous sublayer (Hervouet 2007)], the velocity profile close to the base was defined by a logarithmic law function of the Nikuradse coefficient k_s representing the roughness size. As the base material used for the experiments was plastic, a Nikuradse coefficient of 10^{-5} m was set. For the rigid vertical walls, slip conditions were assumed (i.e., without friction). Tracer concentration gradients were also set to zero for the rigid walls (base and vertical rigid walls). For the turbulent kinetic energy κ and its dissipation rate ε, the boundary conditions defined by Rodi (1984) for rigid walls were applied.

Note that while in other numerical experiments (e.g., Firoozabadi et al. 2009) dense fluid enters the domain through an open-liquid boundary with the slot dimensions, in this study the saline flow rate was determined based on a series of discrete source terms. The number of source terms was determined via the slot dimensions and the domain discretization. This way, the findings of this study can be applied to future field applications (e.g., brine discharges from desalination plants) wherein the saline outflows are typically located within the study domain rather than along boundaries.

As these types of hydrodynamic models and corresponding grid tools are designed and generally configured (e.g., accuracy levels and number of iterations) to model coastal and ocean processes, laboratory tests should be scaled up to prevent numerical problems from emerging. Froude similarity [i.e., the relevant forces are the inertial and gravity forces (Heller 2011)] and mechanical similarity (i.e., geometric, kinematic, and dynamic similarity) are expected to be achieved and thus fewer scale effects are expected to be obtained. However, as the Reynolds number, R, of the case studied was not sufficiently high (i.e., $\mathsf{R} \gg 2000$) to directly neglect the viscous force, a previous sensitivity analysis varying the scale $Sc_{\mathrm{F}} = L_{\mathrm{NUM}}/L_{\mathrm{LAB}}$ (considering the Froude similarity) was performed. Scale factors studied include the following: $Sc_{\mathrm{F}} = 1$; 10; 20; 50; 80; 100; 200; 1000. This analysis showed that after converting all of the results to the same scale, the relative difference of main quantities (concentration and velocity) for the scale-sensitivity cases (at geometrically equivalent locations) was always lower than 2%. This negligible difference attributable to numerical and scale effects shows that Froude similarity can safely be assumed. Thereafter, a $Sc_{\mathrm{F}} = 100$ scale factor was used so that the modeled density currents have similar characteristics to the far field region of brine discharges.

Table 3. Numerical aspects in each of the sensitivity tests considered

Sensitivity tests	Δx	$\Delta z_{\min}$	*Sce*	*Hyd*	TCMh	TCMv	$AdSch_{\kappa\varepsilon}$
Domain discretization	$\Delta x_1 = [bo/20, bo]$ $\Delta x_2 = [bo/4, 3bo]$	$[ho/40, ho]$	Q and V	with	Cst	MLPrandtl	—
Source-input hydrostatic hypothesis	$\Delta x_1 = bo/8$ $\Delta x_2 = bo$	$ho/20$	Q-Q and V	with-without	Cst	MLPrandtl	—
Turbulence	$\Delta x_1 = bo/8$	$ho/20$	Q and V	with	Cst	Cst, ML	Charcs
Modeling	$\Delta x_2 = bo$	—	—	—	Smago	κ-ε	2nd O-KP

Sensitivity Analysis Results and Discussion

Domain Discretization

Appropriate computational grid design is critical to simulate real physical processes while avoiding artificial numerical effects. As a general rule, a fine grid domain discretization (i.e., high resolution) is needed when high spatial-temporal gradients of the variables modeled are anticipated. For negatively buoyant density current flows, high variability areas are the zone closest to the bottom (high vertical gradients) and the surroundings of the discharge location (high vertical and horizontal gradients). This section presents the results of our domain discretization sensitivity tests, in which the horizontal and vertical discretization were varied, leaving the rest of the numerical aspects constant according to Table 3. We note that sigma-layer coordinates are necessary to resolve the vertical structure of the density current. The number of sigma planes and their spacing was therefore investigated as part of the sensitivity tests.

First, sensitivity to the horizontal discretization was studied. For this purpose, vertical discretization close to the bottom was set as $\Delta z = ho/20$, following the recommendations of Kulis and Hodges (2006). As shown in Table 3, two horizontal discretization parameters were defined, namely Δx_1, the highest resolution close to the discharge location, and Δx_2, the lowest resolution in the area furthest away from the discharge location. To compare corresponding patterns of horizontal spreading, Fig. 3(a) shows the front positions versus time in the plane of symmetry and in the plane at 45° relative to the symmetry plane (see lines 0° and 45° of Fig. 2). These spatial and temporal quantities are normalized by the characteristic length and time scales of plume-like behavior flows (Chu and Jirka 1987; Choi and Garcia 2001), $L_p = Q_0^{3/5}/Bf_0^{1/5}$ and $T_p = Q_0^{4/5}/Bf_0^{3/5}$ (Table 1). Furthermore, Figs. 3(b and c) show the longitudinal profile of normalized maximum velocity ($U\max/U_0$) and minimum dilution ($S\min$), respectively, used to analyze the evolution of the density current for the approximate centerline, i.e., where the dilution of the density current is the lowest.

Fig. 3(a) shows that for values of Δx_1 smaller than half of the horizontal slot dimension, i.e., $bo/2$, the spreading converges to similar values for all of the cases. From the longitudinal profile of the normalized maximum velocity shown in Fig. 3(b), higher differences can be observed in the region close to the discharge point. Using the test with the smallest value of Δx_1 as a reference (a value close to the one), it is evident that a discretization of at least $\Delta x_1 < b_0/4$ is needed to capture flow motion in the discharge surroundings. Additional tests varying Δx_2 from $b_0/4$ to $3b_o$ show that in areas positioned far from the discharge location, the horizontal discretization can be coarser and the results do not show significant differences. In this way, the computational time can be minimized, but due to the high levels of horizontal discretization variability, special attention must be paid to the TCMh when it is set as the constant model. In such cases, it is recommended that different eddy viscosity and diffusivity coefficient values are applied along the study domain according the grid resolution (Madsen et al. 1988).

Second, the sensitivity to the vertical discretization was analyzed. Following Kulis and Hodges' (2006) methodology to find the optimal vertical discretization, several tests were conducted both with and without the TCMv for a wide range of vertical discretizations (i.e., wide range of number of layers): $\Delta z_{\min} = [h_0/40, h_0]$. To give computationally efficient simulations, the highest resolution for each case (i.e., the lowest values of Δz, $\Delta z_{\min}$) was established for the region twice the height h_0 from

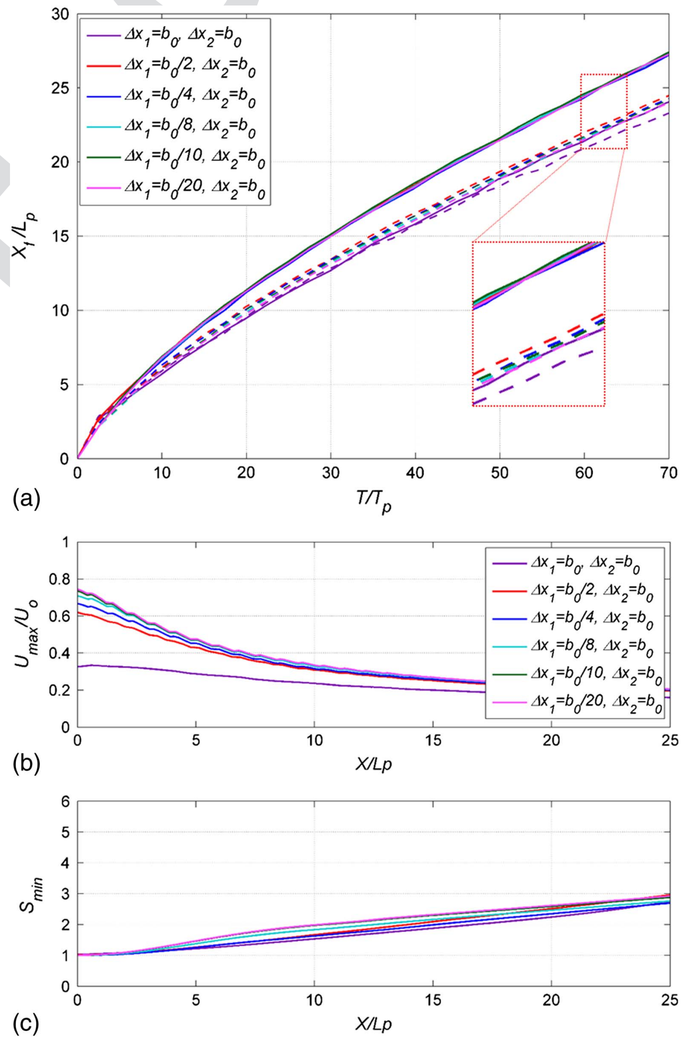

Fig. 3. Horizontal discretization sensitivity tests: (a) dimensionless front position versus dimensionless time for lines 0° (continuous line) and in line 45° (dashed line); (b) longitudinal profile of normalized maximum velocity; and (c) longitudinal profile of minimum dilution.

the base and from that depth to the surface, spacing was gradually increased by a factor of 1.5. The results of these tests (with and without TCMv) were used to evaluate the relationship between global modeled and numerical mixing (i.e., mixing only due to numerical effects not related to the real physics of the process) at different vertical discretizations. For cases in which the TCMv was turned off (no turbulence NT tests), all mixing can be attributed to molecular Brownian motion. As in these NT tests the kinematic viscosity (i.e., molecular) coefficient was set to $10^{-9}\ \mathrm{m^2/s}$, vertical mixing should effectively be zero. Therefore, any mixing observed in the NT tests can be attributed to numerical effects or so-called numerical mixing (or numerical diffusion). Conversely, for cases in which the TCMv was turned on, mixing can be attributed to the combination of turbulent and numerical mixing, henceforth referred to as global modeled mixing. The aim of this specific analysis is to detect the number of layers from which numerical mixing can be considered negligible as compared with the global modeled mixing. Calculating the vertical entrainment coefficient (E) in the symmetrical longitudinal profile (line 0°) for both types of tests generates a quantitative measure for mixing. The entrainment coefficient is calculated from the salinity longitudinal profile using the method developed by Dallimore et al. (2001). This method is based on equations for the conservation of volume (Eq. 8) and solute mass (Eq. 9)

$$\frac{d(Uh)}{dx} = EU \tag{8}$$

$$U\beta h = \text{constant} \tag{9}$$

where U, β, and h are the mean values for velocity, fractional density $[\beta = (\rho - \rho_a)/\rho_a]$ generated from saline concentrations, and the density current thickness for each location, respectively. The value of the current thickness h is defined as the distance from the base where the salinity concentration is less than 10% of the maximum concentration value at the corresponding location. Combining Eq. (8) with Eq. (9) generates equation Eq. (10) where dC/dx is the variation in concentrations when the current travels with the mean velocity. By assuming similarity of the concentration profiles (Parker et al. 1987; Pérez-Díaz et al. 2018), C can be set as proportional to $C_{\max}$

$$E = -\frac{h}{C}\frac{dC}{dx} = -\frac{h}{C_{\max}}\frac{dC_{\max}}{dx} \tag{10}$$

Fig. 4 shows the value of the average normal entrainment coefficient E_N relative to the number of vertical layers within the density current $N_{Zh} = h_0/\Delta z_{\min}$ for different horizontal discretizations and for both kind of tests, namely with and without the application of the TCMv. The variable E_N represents a single average value calculated from $X/L_P = 15$ to eliminate the effects of the density current‘s initial adjustment on the normal flow state.

Fig. 4 reveals that with the exception of those for the most coarsely resolved tests, the global modeled entrainment rates (i.e., entrainment rates of cases with the TCMv set to ML) converge on the order of 10^{-2} while numerical entrainment rates (i.e., entrainment rates of cases with the TCMv turned off, NT) decrease nearly exponentially as the vertical resolution increases. For tests involving values of $h_0/\Delta z_{\min}$ higher than 8, the difference between the two entrainment rates reaches close to or higher than an order of magnitude of 10^{-2} (specifically, for $h_0/\Delta z_{\min} = 8$, global modeled entrainment rates are less than 1.2×10^{-2} and numerical rates are higher 4×10^{-3}). Thus, for cases involving more than eight layers within the density current ($N_{zh} = h_0/\Delta z_{\min} > 8$), numerical mixing ceases to dominate global modeled mixing. We note that when

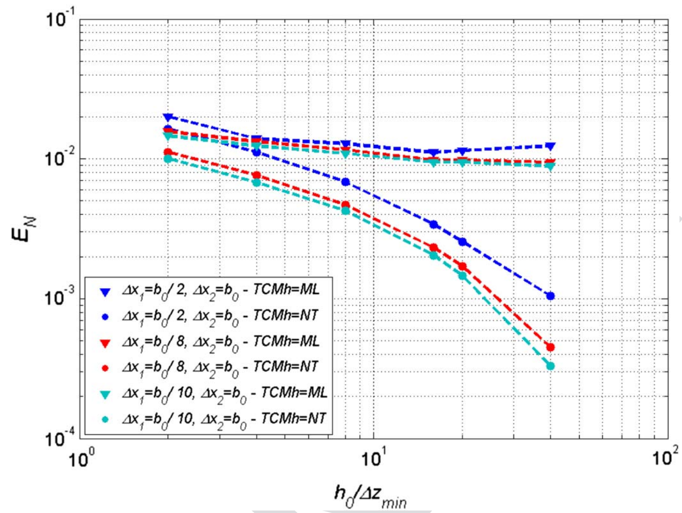

Fig. 4. Vertical discretization sensitivity tests showing normal entrainment versus vertical discretization for different horizontal discretizations.

considering the horizontal resolution sensitivity tests for the each of the corresponding number of layers, the previous pattern is maintained and always generates higher entrainment rates for tests involving coarser horizontal resolutions. Fig. 4 shows that both horizontal and vertical resolutions affect the global modeled mixing; the higher the resolution, the lower the degree of numerical diffusion. To ensure that the effects of numerical diffusion are negligible, our testing shows that $h_0/\Delta z_{\min}$ values of 16–20 are needed. As shown in Fig. 4, this ensures rates of numerical diffusion that are approximately an order of magnitude below the global modeled mixing.

Source Input and Hydrostatic Hypothesis 533

Having defined a suitable computational grid, numerical aspects that can also affect the initial region of the density current are studied. As cited in the numerical model description, the TELEMAC-3D model allows both hydrostatic and nonhydrostatic pressure fields to be assumed. The hydrostatic assumption is mainly valid for anisotropic flows for which scales of motion are substantially larger in the horizontal than in the vertical. As density currents are primarily horizontal flows, the hydrostatic hypothesis should be appropriate. However, as Mahgoub et al. (2015) show, vertical accelerations may not be negligible relative to gravitational acceleration for the starting region of the density current due to local effects found in the near field region. Numerically, with a nonhydrostatic pressure field, the vertical momentum equation is fully solved without simplification, and the pressure equation is split up into hydrostatic pressure and a dynamic pressure terms. TELEMAC-3D also allows the specification of a liquid flow rate Q an injection velocity V. This section presents our analysis of the effects of these numerical aspects on the density current behaviour. The numerical parameters for these simulations are presented in Table 3.

Note that while physically there is only one source of $h_0 \times b_0$ dimensions, due to domain discretization, it is numerically transformed in several discrete source terms. For instance, 160 discrete sources of a liquid flow rate of $Q_0/160$ are needed for the specifications shown in Table 3 ($\Delta x_1 = bo/8$ and $\Delta z_{\min} = ho/20$).

Fig. 5 shows the effects of the source specification type and pressure formulation (i.e., hydrostatic hypothesis) on the horizontal

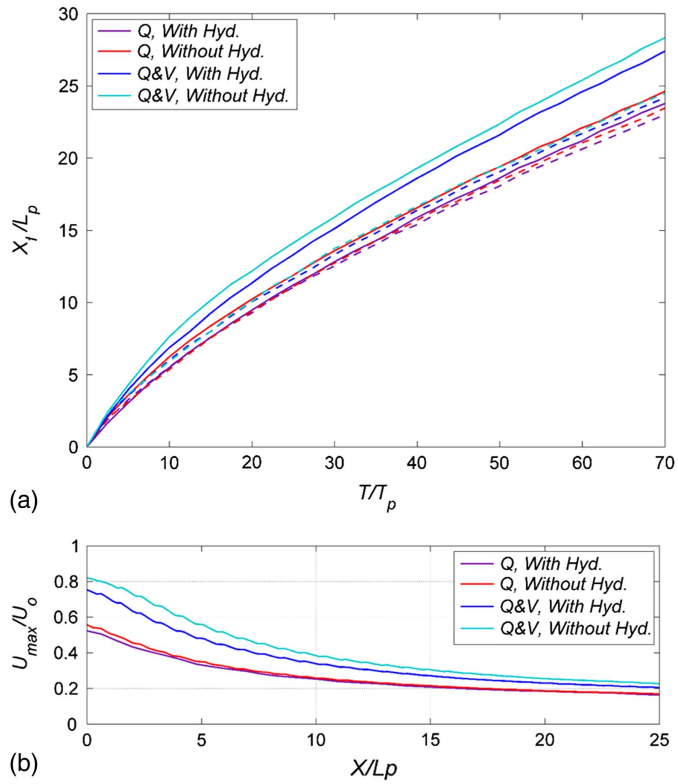

Fig. 5. Source-input and hydrostatic-hypothesis sensitivity tests: (a) dimensionless front position versus dimensionless time for lines 0° (continuous line) and 45° (dashed line); and (b) longitudinal profile of normalized maximum velocity.

spreading and the symmetrical longitudinal profiles of maximum velocity. As is shown for the source specification, Q and V information is needed to capture flow motion in the discharge surroundings, obtaining $U_{\max}/U_o$ values closer to 1. Consequently, horizontal spreading rates for cases involving injection velocity [Fig. 5(a)] are higher. The assumption of the hydrostatic pressure has a lesser impact, but tests with nonhydrostatic pressure generate values of $U_{\max}/U_o$ of closer to 1. Nevertheless, the present study found that the nonhydrostatic simulations required an additional smoothing to be applied to the free surface elevation solution to reduce oscillations. Further study would be required to optimize the nonhydrostatic model configuration, if it were required for a particular application. However, for the present application, differences between the nonhydrostatic and hydrostatic solutions were not considered to be significant. Furthermore, the solution of the more complex system of equations increased computation times by a factor of 1.5–2 for the density current simulations. Therefore, the hydrostatic pressure formulation is considered to be most appropriate, and is likely to give more acceptable simulation times for field-scale applications involving more complex environmental conditions.

Turbulence Modeling

Based on the previous sensitivity tests, this section presents findings derived from the application of well-known TCMs briefly described in the previous section: constant, Smagorinsky, mixing length, and κ-ε. Table 3 summarizes both the fixed numerical aspects (Δx, Δz, Sce, and Hyd) and options considered for this sensitivity test (TCMh, TCMv, and $AdSche_{\kappa\varepsilon}$).

For the turbulence closure model of the horizontal direction (TCMh), it is common for hydrodynamic models to use a constant turbulence model. Thus, the user must calibrate the horizontal eddy viscosity value ν_{th} depending on the particular flow being studied and depending on domain discretization (Madsen et al. 1988). However, in taking advantage of options programmed into TELEMAC-3D, simulations varying the TCMh between the constant and Smagorinsky models were compared. For the studied case, while using the Prandtl mixing length TCMv, no appreciable differences were observed in the results. For these tests, ν_{th} was defined according to the variable grid resolution (applying scaled-down absolute values of 4.7×10^{-5} to $1.6\,10^{-4}$ $\mathrm{m/s^2}$), and the calibration parameter of the Smagorinsky model (C_s) was defined as 0.1, a common value for anisotropic flows (e.g., flow in a canal). The κ-ε model was also set as the TCMh model, but in this case the κ-ε model was mandatory for the TCMv, and so the influence of the TCMh could not been extracted. In addition, the simulations became so time-consuming and unstable (due to numerical problems found at open liquid boundaries based on Neumann boundary conditions for the κ and ε equations) that this option for the TCMh was not considered.

Due to the strong stratification associated with density currents, the turbulence closure model of the vertical direction (TCMv) is a key numerical aspect for accurately predicting their behavior. To analyze the TCMv's influence on the vertical structures of the flow, Figs. 6–8 show downstream variations in the velocity (the main velocity component, U_x) and salinity (C) cross profiles found along the symmetry plane (see line 0° of Fig. 2) for each TCMv case in the constant, mixing length, and κ-ε models. For all of the simulations, the TCMh is held as constant according to the results presented previously. Furthermore, these figures present normalized cross profiles that collapse into a single profile, called a similarity profile (Ellison and Turner 1959; Parker et al. 1987; Garcia 1993). In addition to our numerical results, measured data obtained via PIV-PLIF techniques are also displayed.

Fig. 6 shows cross profiles derived from different simulations with constant TCMv based on varying ν_{tv} values of $\nu_{th}/1000$ to $\nu_{th}/10$. In these simulations the eddy diffusivity value Γ is defined by the Schmidt number ($\sigma_c = \nu_{tv}/\Gamma_v$), which is considered to take values of close to one for these types of flows. Both the velocity and salinity concentration cross profiles show that the simulation $\nu_{tv} = \nu_{th}/10$ better fits the experimental data. However, the simulation does not represent the approximate shape of the first cross sections, i.e., those with higher momentum and concentration values. For the remainder of the cross sections, the velocity agrees with the experimental data while the dilution is underestimated (i.e., higher concentrations than were expected). As is shown by the similarity cross profiles, the normalized mean horizontal velocity and mean concentration cross profiles collapse well into single profiles, which agree with the experimental similarity profiles.

Fig. 7 shows cross profiles for the TCMv mixing length models (both the Prandtl forumation and the Nezu and Nakagawa formulation). For these cases, the damping function addressed by Munk and Anderson (1948) is used to govern vertical mass and momentum exchanges. The results of the two simulations are almost identical, showing logarithmic velocity and concentration profiles for the most parts of the density current body. In these cases, the profiles are the result of agreement between the ML model, the damping function and the turbulence model for the bottom based on the previously defined roughness size (i.e., the Nikuradse coefficient). While the velocity cross profiles match fairly well with experimental data for the whole density current body, the concentration profiles significantly underestimate dilution levels found in the region close to the bottom for areas located closer areas to the discharge.

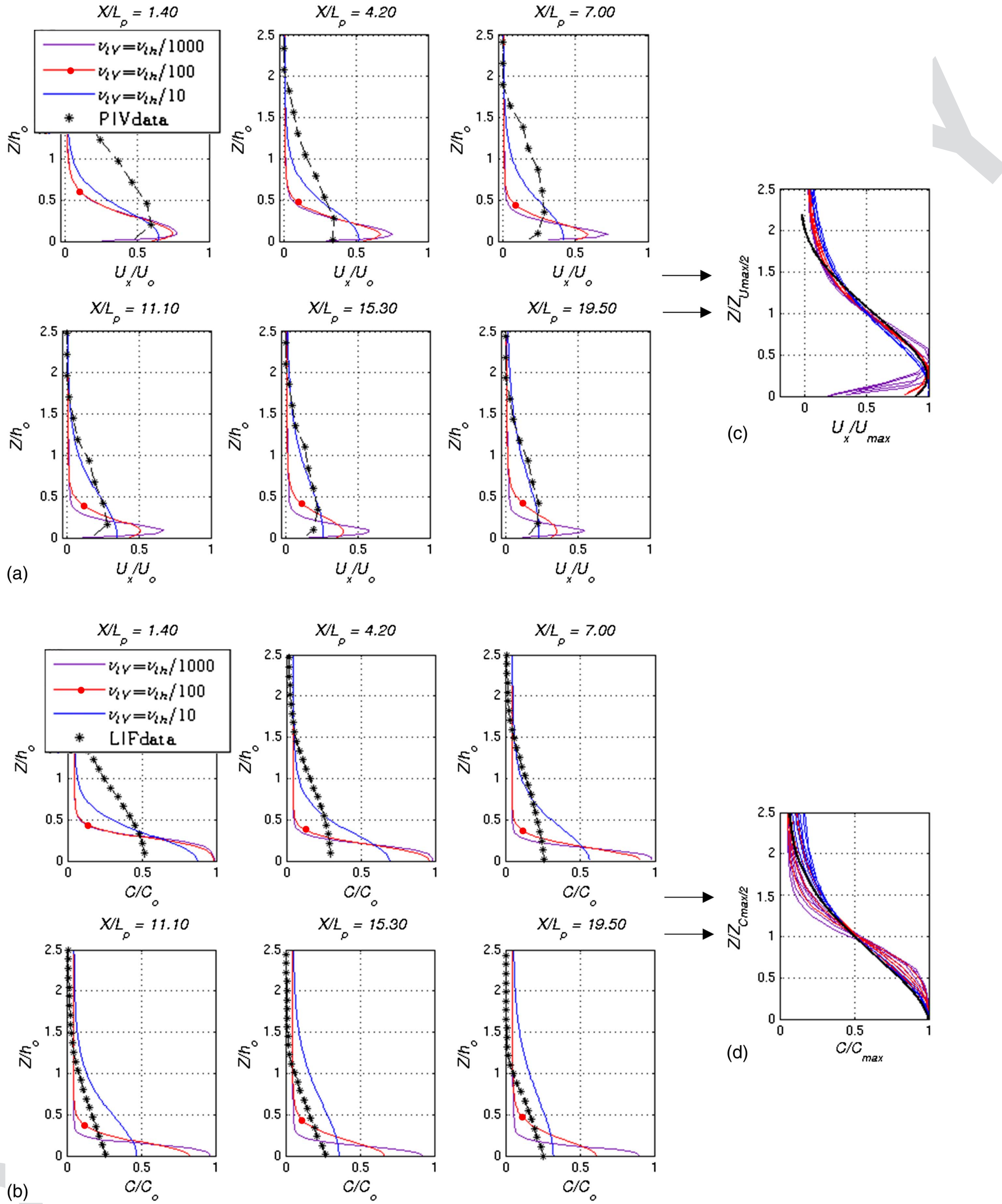

Fig. 6. Downstream variation cross profiles for cases with TCM$v = Cst$: (a) horizontal velocity; (b) salinity concentration; and the corresponding similarity cross profiles for (c) horizontal velocity; and (d) salinity concentrations.

In addition, the normalized mean horizontal velocity and mean concentration cross profiles collapse into single profiles but they disagree with the experimental similarity profiles. This shows that the presented TCMv option does not capture the vertical shape of the analyzed density current.

Fig. 8 shows the cross profiles derived from two simulations with the κ-ε TCMv applied. The two simulations differ in terms of advection scheme ($AdSch_{\kappa\varepsilon}$) applied. Whereas in one case the method of characteristics was used, for the other case the most conservative scheme programmed into the TELEMAC-3D was

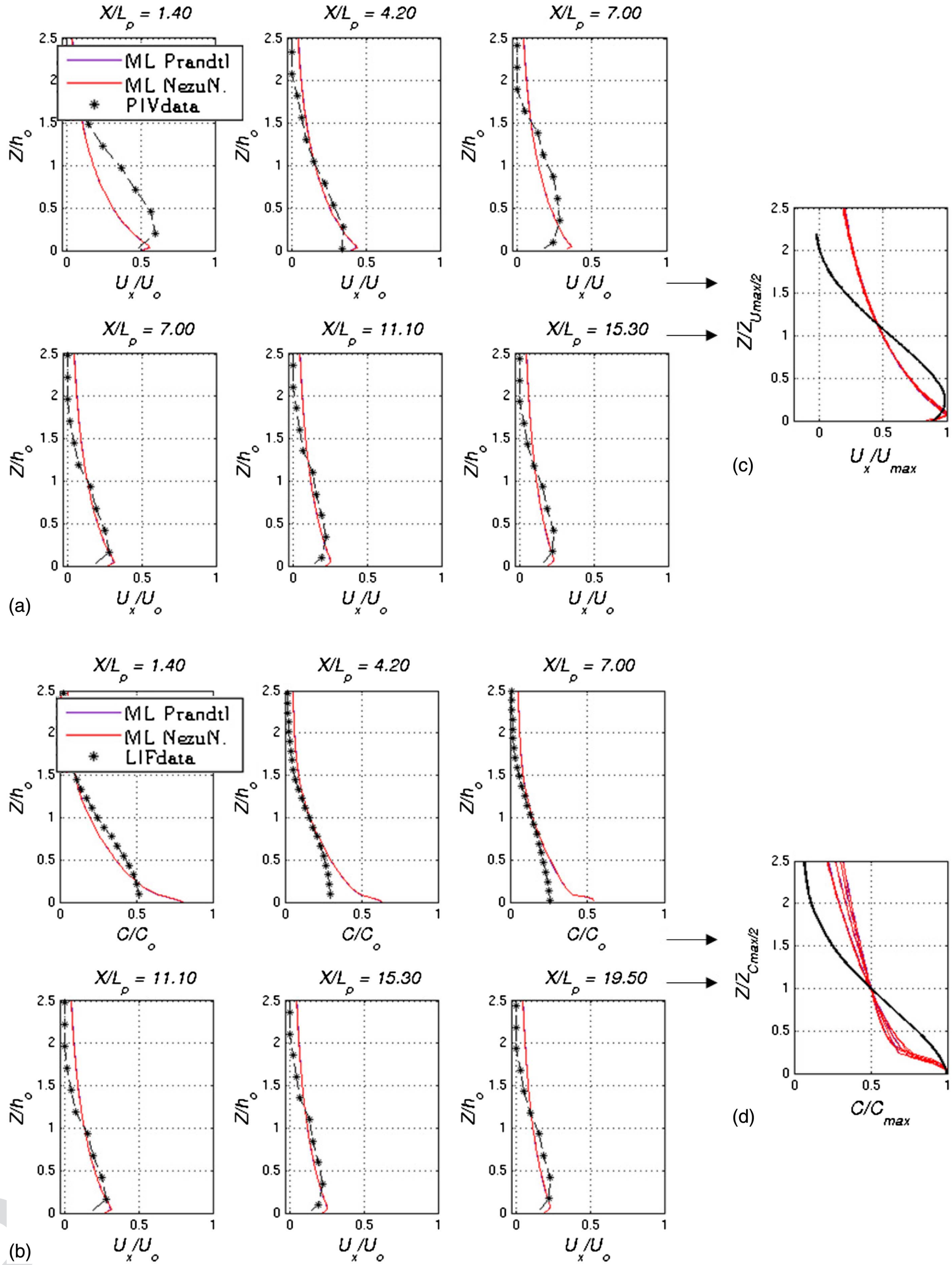

Fig. 7. Downstream variation cross profiles for cases with TCM$v = ML$: (a) horizontal velocity; (b) salinity concentration; and the corresponding similarity cross profiles for (c) horizontal velocity; and (d) salinity concentrations. Note that both lines overlap in all figures.

used (2nd-KP). The characteristic method is recommended by LNHE (2007), as it has provided satisfactory results in many instances and is the most efficient. Nevertheless, due to the unique nature of these types of flows, where the buoyancy force is a driven force, i.e., the accurate definition of the mass-tracer quantities is fundamental, the authors deemed it necessary to distinguish effects of the advection scheme. Fig. 8 shows that both simulations overestimate the velocities and concentrations close to the bottom for all

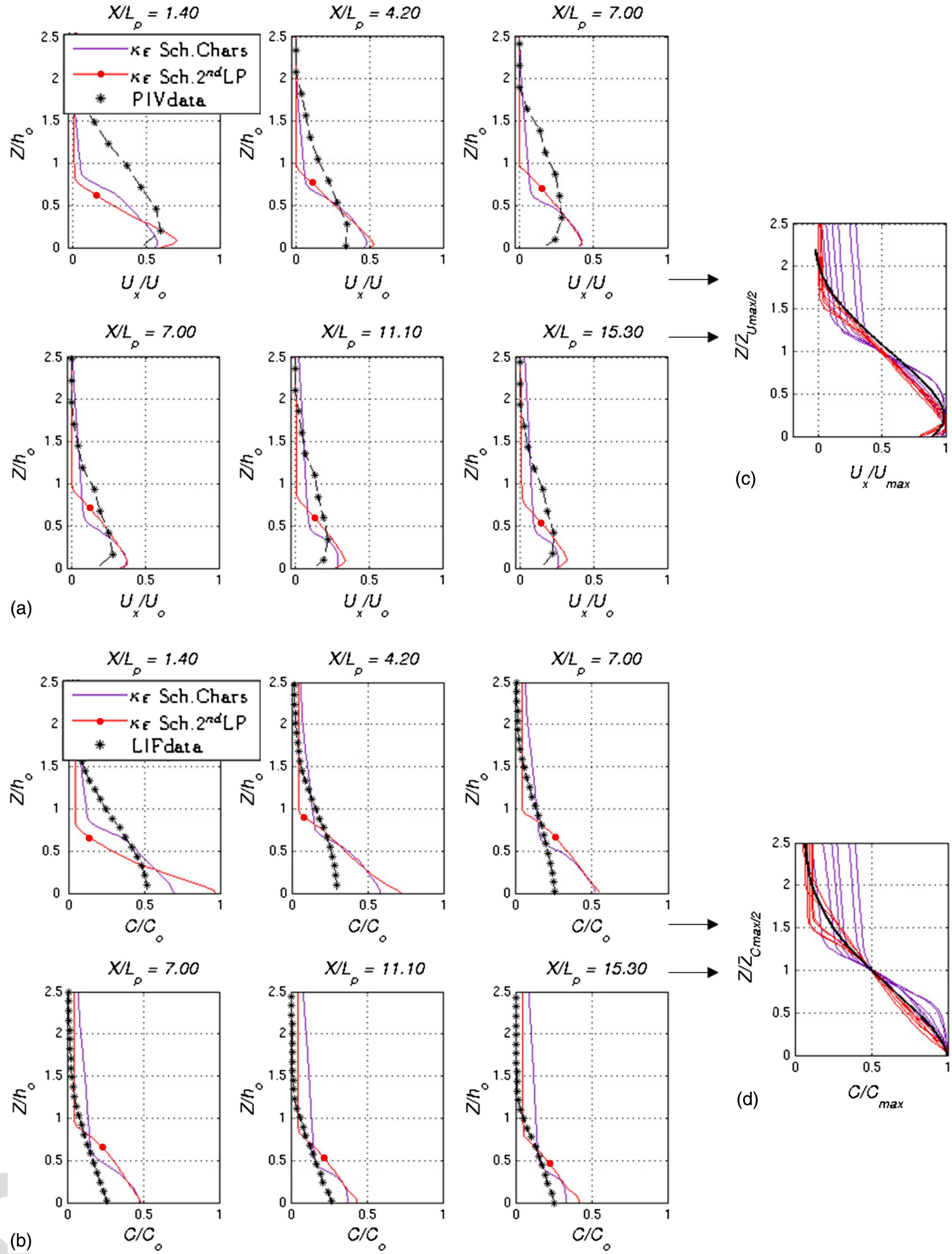

Fig. 8. Downstream variation cross profiles for cases with TCM$v = \kappa$-ε: (a) horizontal velocity; (b) salinity concentration; and the corresponding similarity cross profiles for (c) horizontal velocity; and (d) salinity concentrations.

of the locations studied, although the shape of the profile obtained is noticeably different from one case to the other. Regarding the similarity profiles, from which a proper shape comparison can be undertaken, they show that the simulation applying the most conservative advection scheme presents better agreement with the experimental similarity curves.

Taking the similarity cross profiles into account, i.e., the profile shape profile, the constant, and the κ-ε TCMv are the models that best capture the vertical structure of the density current. As the constant model only uses ν_{tv} as a calibration parameter and as the results presented in Fig. 6 for $\nu_{tv} = \nu_{th}/10$ are its best results, we focus on the κ-ε TCMv. As described in the previous section, the κ-ε model includes several empirical constants obtained via data fitting for a broad range of flows. Of these empirical constants, the $c_{3\varepsilon}$ and c_μ affect the modeling of density currents, and their values have been the subject of debate. Hossain and Rodi (1982), Rodi (1987), and Choi and Garcia (2002) have suggested that $c_{3\varepsilon}$ values of 1–0.6 show a good agreement with experimental results for density currents. Conversely, the standard value of the other controversial empirical constant ($c_\mu = 0.09$) was used on the basis of experiments on flows for which production P and dissipation ε of the turbulence energy were in approximate balance. For weak shear flows (e.g., far-field jets and plumes for which the velocity difference across the flow represents only a small fraction of the convection velocity), P was found to be significantly different from ε, and c_μ was found to take different values (Rodi 1975). Rodi (1972) correlated experimental data and proposed a function of $c_\mu = f(\overline{P/\varepsilon})$ that is only valid for thin shear layers (similar to the density currents studied).

To study effects of these empirical constants on density currents modeling, the results of several simulations varying the values of these constants are analyzed. The range of values for $c_{3\varepsilon}$ and c_μ were chosen based on state-of-the-art findings, namely $c_{3\varepsilon}$ values of 1–0.6 and c_μ values of 0.09–2.5. Another important parameter is the Schmidt number σ_c, which contributes to the eddy diffusivity definition and which is valued at between 0.7 and 1. However, due to its lesser impact on the results compared to the $c_{3\varepsilon}$ and c_μ constants' impact, it was assumed to be equal to 0.7, a common value for heat and salinity transport. Based on the experimental results, comparisons are drawn with results obtained from different simulations using the root mean-square absolute error (RMSE) formula

$$\mathrm{RMSE} = \sqrt{\frac{1}{N}\sum_{i=1}^{N}(x_{exp} - x_{num})^2} \tag{11}$$

where x_{exp} = experimental values of the variable studied (in this case the salinity concentration and horizontal velocity); x_{num} represents the corresponding numerical value; and N = number of pairs of comparable values. In this case, due to the large amount of data obtained from the PIV-PLIF experiments, N corresponds to the number of cross profiles multiplied by the number of data points measured within the density current thickness (which varies depending on the variable). To estimate the relative error, the normalized RMSE (NRMSE) was obtained by dividing the RMSE by the initial value of the evaluated magnitude (C_0 or U_0) and by multiplying this value by 100 to obtain the percentage. As a calibration assessment, the error obtained for each simulation while varying the $c_{3\varepsilon}$ and c_μ constants is shown in Table 4.

Table 4 shows that the results of the simulation with $c_{3\varepsilon}$ equal to 0.7 and c_μ equal to 0.2 offer the smallest errors, namely 0.135 psu for salinity and 0.005 m/s for velocity (2.8% and 4.8%, respectively). Fig. 9 shows the downstream variation and similarity cross profiles for the simulation. As is shown, the numerical and experimental data agree fairly well, both in terms of shapes and absolute values.

The optimal value of $c_{3\varepsilon}$ obtained from this study (~[0.7 − 0.6]) agrees with the values published in the scientific literature on density currents (e.g., Hossain and Rodi 1982; Rodi 1987; Choi and Garcia 2002). Note that certain researchers define the empirical constant as $(1 - c_{3\varepsilon})$ rather than as $c_{3\varepsilon}$ so that the corresponding optimum value is then (~[0.3 − 0.4]). Conversely, the optimum value of c_μ obtained (~0.2) is included within the range of values established by function $c_\mu = f(\overline{P/\varepsilon})$, defined by Rodi (1972). This function is only valid for thin shear layers such as density currents where the argument $\overline{P/\varepsilon}$ is the average value of P/ε across the layer. Launder et al. (1973) showed applying this function significantly improves the κ-ε model's capacity to predict such flows. Far from the standard value ($c_\mu = 0.09$), which is accepted for flows involving the production P and dissipation ε of turbulent kinetic energy in balance ($\overline{P/\varepsilon} \simeq 1$), the optimum value obtained corresponds to a $\overline{P/\varepsilon}$ value of ~0.5. Rather, the average production term is approximately half the average dissipation of turbulent kinetic energy. Fig. 10 shows downstream variations of terms involved in κ-ε equations, such as P and ε described previously.

For the graphs plotted in Fig. 10, the horizontal gradient of vertical velocity ($\partial U_Z/\partial X$), the vertical gradient of horizontal velocity ($\partial U_X/\partial Z$) and the vertical eddy viscosity (ν_{tv}) are extracted to obtain the production term (P) following Eq. (4). Small values of $\partial U_Z/\partial X$ were anticipated due to the horizontal nature of the flow studied, and the range of values ($[-2, 3]\ 1/s$) obtained for $\partial U_X/\partial Z$ agrees well with the experimental data ($[-2, 2]\ 1/s$). As was expected, the eddy viscosities reduce according to the velocity decay. Fig. 10(d) presents the production term (P), which shows very small values close to the bottom compared to the dissipation of turbulent kinetic energy (ε), plotted in Fig. 10(f). Finally, the turbulent kinetic energy (κ) is shown in Fig. 10(e). The shape of the κ cross profiles and their order of magnitude (10^{-5}) match with the experimental horizontal Reynolds stress component (the main component of turbulent kinetic energy in such horizontal flows, $\tau_{XX}/\rho U_X^2$). The κ cross profiles present a clear peak corresponding with the upper flow boundary and a zone of minimum turbulence energy at the location presenting highest velocity, which is consistent with Gray et al. (2006), Islam and Imran (2010), and Gerber et al. (2011).

Table 4. Calibration of empirical coefficients c_μ and $c_{3\varepsilon}$ of the κ-ε model

κ-ε coefficients		Salinity errors		Velocity errors	
$c_{3\varepsilon}$	c_μ	RMSE (psu)	NRMSE_{C_0} (%)	RMSE (m/s)	NRMSE_{U_0} (%)
1	0.09	0.496	10.3	0.012	11.7
	0.15	0.396	8.2	0.011	10.5
	0.2	0.244	5.0	0.008	7.96
	0.25	0.253	5.3	0.008	8.2
0.9	0.096	0.45	9.4	0.01	10.2
	0.15	0.358	7.5	0.01	9.8
	0.2	0.21	4.4	0.007	7.2
	0.25	0.219	4.6	0.007	7.5
0.8	0.09	0.427	8.9	0.011	10.6
	0.15	0.318	6.6	0.009	9.0
	0.2	0.177	3.7	0.007	6.7
	0.25	0.187	3.9	0.006	6.4
0.7	0.09	0.318	6.6	0.008	8.3
	0.15	0.199	4.1	0.007	6.8
	0.2	0.135	2.8	0.005	4.8
	0.25	0.139	2.9	0.006	5.6
0.6	0.09	0.355	7.4	0.009	9.0
	0.15	0.238	4.9	0.007	7.3
	0.2	0.137	2.8	0.006	5.7
	0.25	0.14	2.9	0.006	5.7

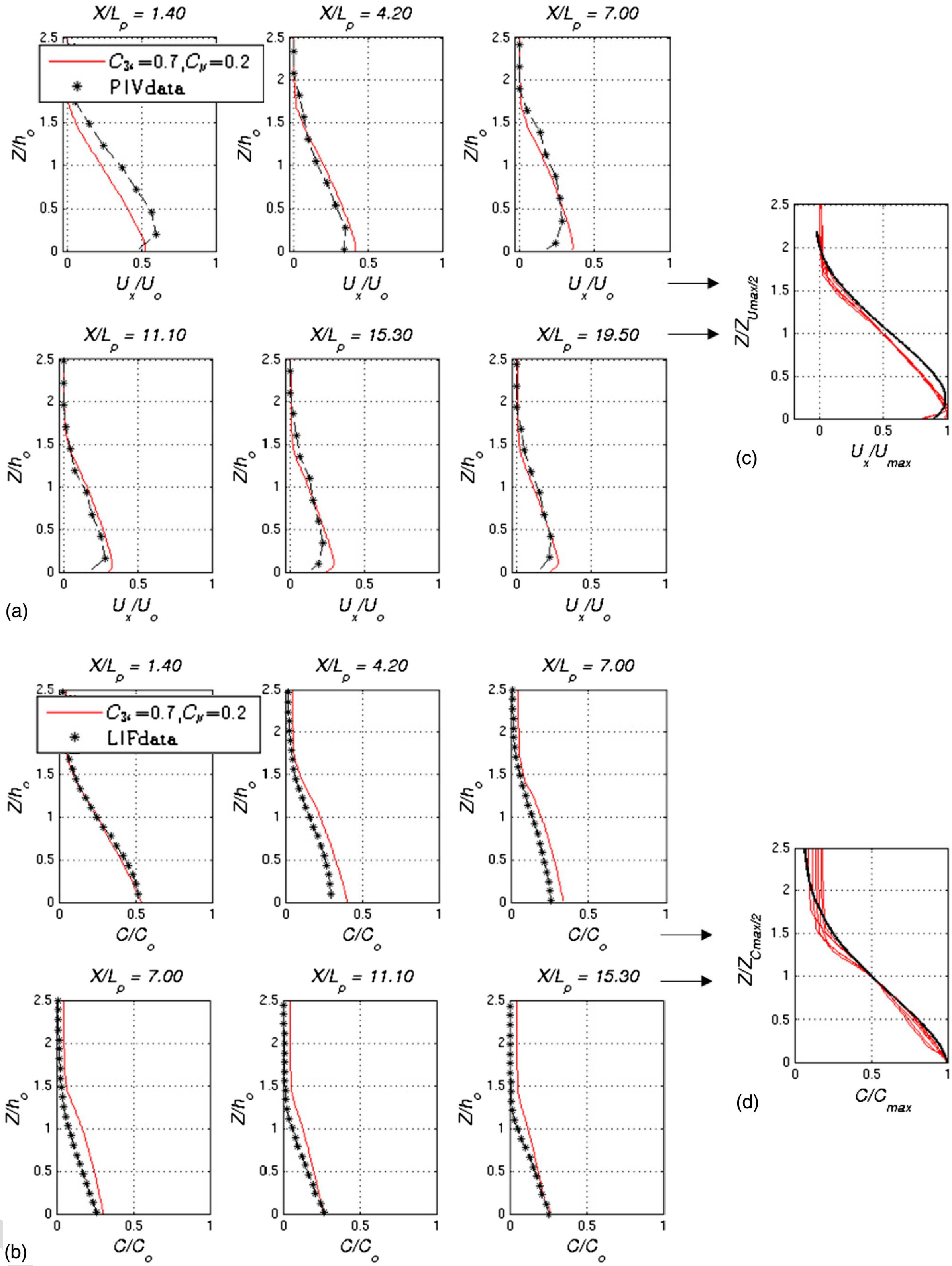

Fig. 9. Downstream variation cross profiles for cases with calibrated TCM$v = \kappa$-ε: (a) horizontal velocity; (b) salinity concentration; and the corresponding similarity cross profiles for (c) horizontal velocity; and (d) salinity concentrations.

Validation Results

Based on the previous sensitivity analysis, a proposed modeling setup to simulate the behaviour of density currents is shown in Table 5. Apart from the previously calculated relative errors regarding the evolution of main variables in the cross profiles, in applying these recommendations to Case 1, a relative error of the front position ($\mathrm{NRMSE}_{X_{f}exp}$) of less than 6% is obtained. For the evolution of the density current in the streamwise direction, wherein the dilution of the current is the lowest (line 0°),

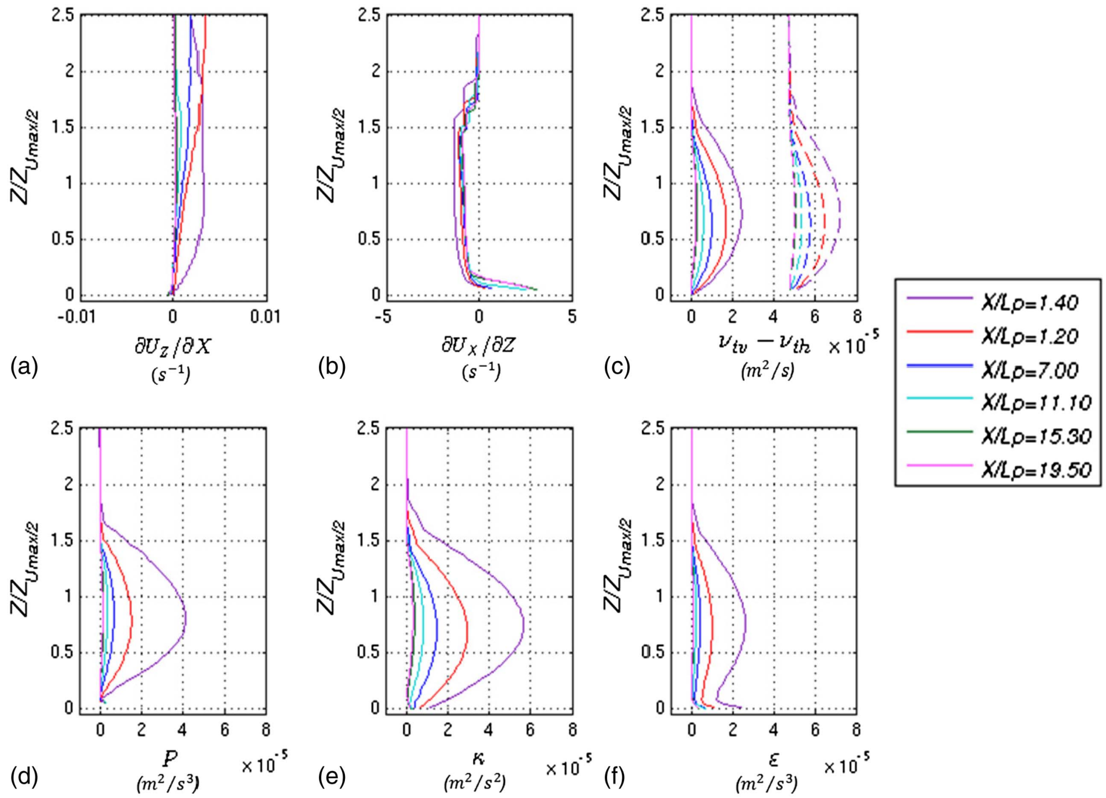

Fig. 10. Downstream variation of the terms involved in κ-ε Eqs. (2) and (3) for the calibrated test: (a) horizontal gradient of vertical velocity; (b) vertical gradient of horizontal velocity; (c) horizontal (dashed line) and vertical (continuous line) eddy viscosities; (d) production term; (e) turbulent kinetic energy; and (f) dissipation of turbulent kinetic energy.

Table 5. Optimal numerical aspects for predicting density currents

Numerical parameter	Optimum
Δx	$\Delta x_1 \leq bo/4$
Δz	$\Delta z_{\min} \leq ho/16$
Sce	Q and V
Hyd	with
TCM*h*	Cst
TCM*v*	κ-ε ($c_\mu = 0.2$, $c_{3\varepsilon} = 0.7$)
$AdSch_{\kappa\varepsilon}$	Most conserv.(p.e., 2nd O-KP)

the error is roughly 4% for the main velocity component (NRMSE_{U_0}) and is less than 1.3% for the dilution ($\mathrm{NRMSE}_{S_{\min}}$) value. Fig. 11 illustrates the evolution of the main variables described (i.e., the front position, the dilution, and the main velocity component) and their graphical comparison with the experimental data. Moreover, Fig. 12(a) presents the good agreement between the numerical and experimental spreading results for different times using a plan-view comparison of concentration values. The longitudinal symmetry profile views of the numerical and experimental concentration results are shown in Figs. 12(b and c), for consistency with the previous results presentation.

To ensure that the proposed modeling setup is valid for density currents generated under different flow conditions, considering turbulent flow and supercritical regime (i.e., R>1000 and F>1), it was applied to the complete set of experimental density currents (Table 1). Comparisons were made between the experimental and numerical results from the minimum dilution obtained from the last section of density currents (S_{minF}), which represents the result of the transport and mixing processes and the parameter on which the environmental regulations are commonly based. Table 6 shows the comparison between the experimental and numerical results, with subindices E and N, respectively. As is shown, a good agreement between the experimental and numerical values was obtained for all cases. Furthermore, the modeled values S_{minF_N} maintain the correlation revealed by the experiments S_{minF_E}. That is, establishing the value of C1 as the base case $S_{\mathrm{minF}_{Nb}}$ (corresponding to the case analyzed in the sensitivity analysis), the rates $S_{\mathrm{minF}_N}/S_{\mathrm{minF}_{Nb}}$ agree with the corresponding experimental ratio $S_{\mathrm{minF}_E}/S_{\mathrm{minF}_{Eb}}$, showing that steeper slopes (C4 and C5) and higher initial momentum values (C2 and C3) enhance the dilution rate in contrast to the case involving higher initial buoyancy (C6).

Further validation was carried out using the experiments of Choi and Garcia (2001) (see description on experimental database section and on Table 1 of Choi and Garcia 2001). Fig. 13(a) shows that the predicted evolution of the dimensionless half-width ($b_{1/2}$) agrees well with the experimental data. In addition, Fig. 13(b) compares longitudinal spreading values based on front velocity evolution. In this case, velocity is fairly well reproduced when the initial high momentum region is developed. Beyond this comparison, conclusions regarding effects of the different densities and slopes on the described behavior can be drawn from the graphs. In agreement with previous studies (Choi and Garcia 2001; Alavian 1986), steeper slopes favor rapid longitudinal spreading and hinder lateral spreading (i.e., higher front velocities and lower half-widths), and a higher density difference favors longitudinal and lateral spreading (i.e., higher front velocities and higher half-widths).

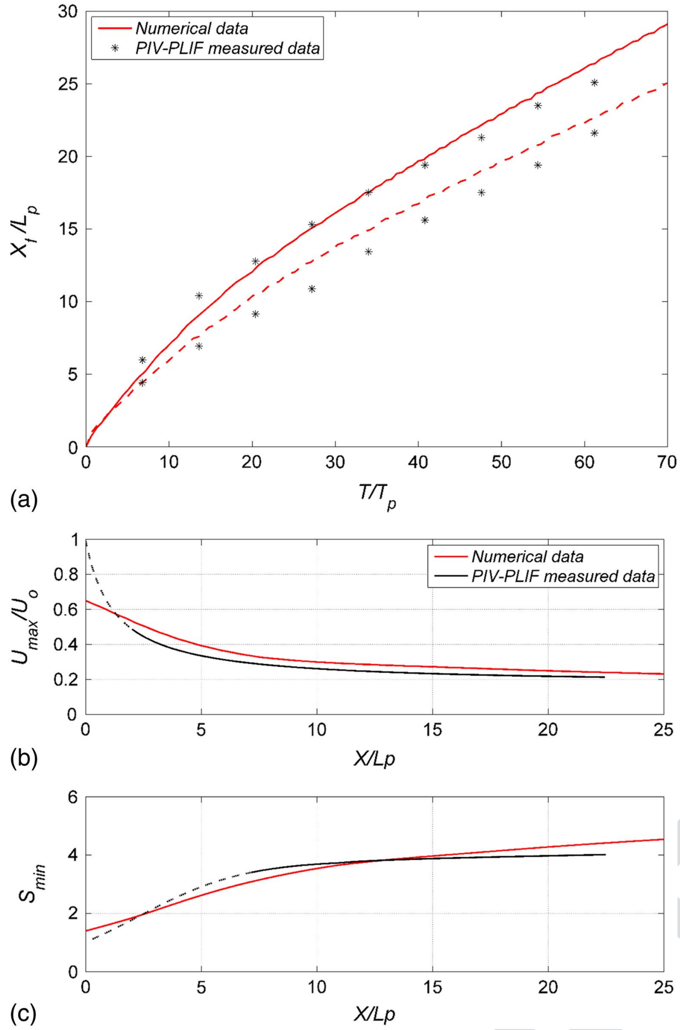

Fig. 11. Comparison between the numerical and the experimental results: (a) dimensionless front position versus dimensionless time for lines 0° (continuous line) and 45° (dashed line); (b) longitudinal profile of normalized maximum velocity; and (c) longitudinal profile of minimum dilution.

Conclusions

Through a comprehensive sensitivity and validation analysis based on the reproduction of several laboratory-generated density currents, this study shows that suitably configured 3D hydrodynamic models can simulate the behavior of saline density currents with a high level of accuracy. Moreover, as these laboratory-generated currents were scaled up to prevent numerical effects and to have similar characteristics to the far field region of brine discharges, the sensitivity and validation analysis as well as the recommendations resulted are extended to real field-scale saline current flows. The main numerical guidelines for solving such flows using these models are as follows:

- Variable spacing horizontal discretization (e.g., unstructured grids) is recommended as a means to obtain high resolutions close to the source. In this way, a lower resolution can be set to the farthest region of the source, rendering application more computationally efficient. Assuming a slot-shaped source ($b_0 \times h_0$), a common approximation for the beginning of the far field region of brine discharges, minimal spacing of at least equal to the width of the slot b_0 must be applied to ensure the momentum and mass conservation as much as possible. Specifically, for the cases analyzed in this study, a spacing of greater than $b_0/4$ is recommended.
- In the vertical direction, a high resolution must be applied to minimize vertical numerical diffusion. For the type of density currents studied in this study and considering the a slot-shaped source, vertical spacing should be at least $h_0/16$. As this fine resolution cannot be maintained along the entire water column (i.e., there would be too many numbers of layers), gradual vertical spacing with the highest resolution close to the bottom (within the density current body) is recommended. In such cases, a sigma layer coordinate (i.e., terrain following) for vertical domain discretization should be applied to keep the finest layers at the bottom.
- Full momentum source specification is advisable, i.e., both flow rate and velocity information (Q and V) should be detailed.
- The hydrostatic hypothesis is considered to be appropriately assumed, as it significantly (1.5–2 times) reduces computation time and because not applying this hypothesis does not generate significantly improved results.

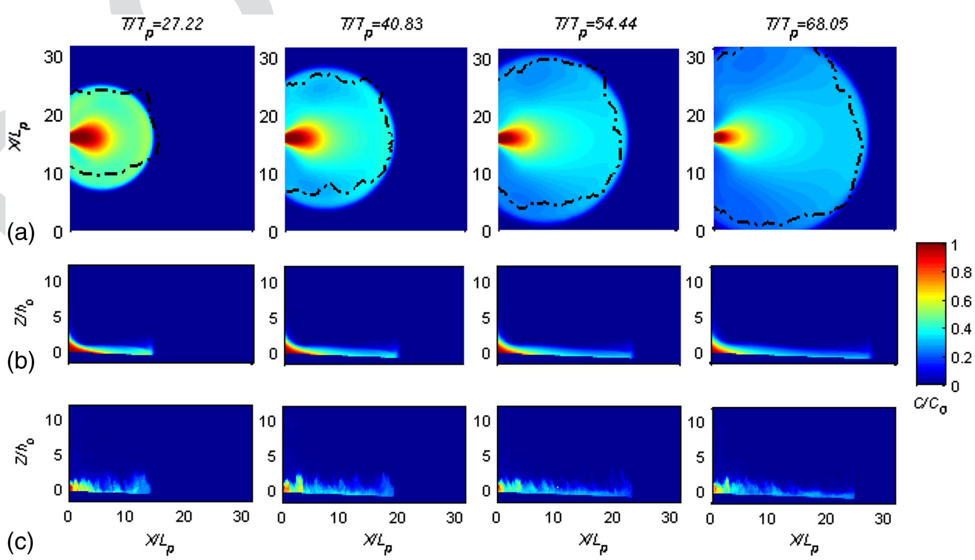

Fig. 12. Comparison between the numerical and the experimental spreading results for different times: (a) plan view (experimental results are shown as the dashed line); (b) profile view of the modelled results; and (c) profile view of the LIF experimental results.

Table 6. Minimum dilution comparison for the last section of the studied density currents

Cases	Modified parameter	S_{minF_E}	S_{minF_N}	$S_{\mathrm{minF}_E}/S_{\mathrm{minF}_{Eb}}$	$S_{\mathrm{minF}_N}/S_{\mathrm{minF}_{Nb}}$
C1	—	4.3	4.5	$S_{\mathrm{minF}_{Eb}}$	$S_{\mathrm{minF}_{Nb}}$
C2	h_0	7.2	7.2	1.66	1.60
C3	Q_0	6.8	5.8	1.56	1.28
C4	α	5.3	5.9	1.23	1.31
C5	α	6.6	6.8	1.525	1.51
C6	$(\rho_a - \rho_0)$	4.1	3.74	0.94	0.83

- The constant model is recommended as a horizontal turbulence closure model (TCMh) varying eddy coefficient values according to the grid resolution.
- Several vertical turbulence closure models (TCMv) such as constant, mixing length, or κ-ε models can be successfully applied. However, given the demonstrated influential role a TCMv has on the numerical simulation of such flows, calibration should be applied to each case study. Specifically, for the cases analyzed in this study, the calibrated κ-ε model (empirical constants $c_{3\varepsilon}$ and c_μ are equal to ~0.7 and ~0.2, respectively) in conjunction with the most conservative advection scheme for κ-ε equations

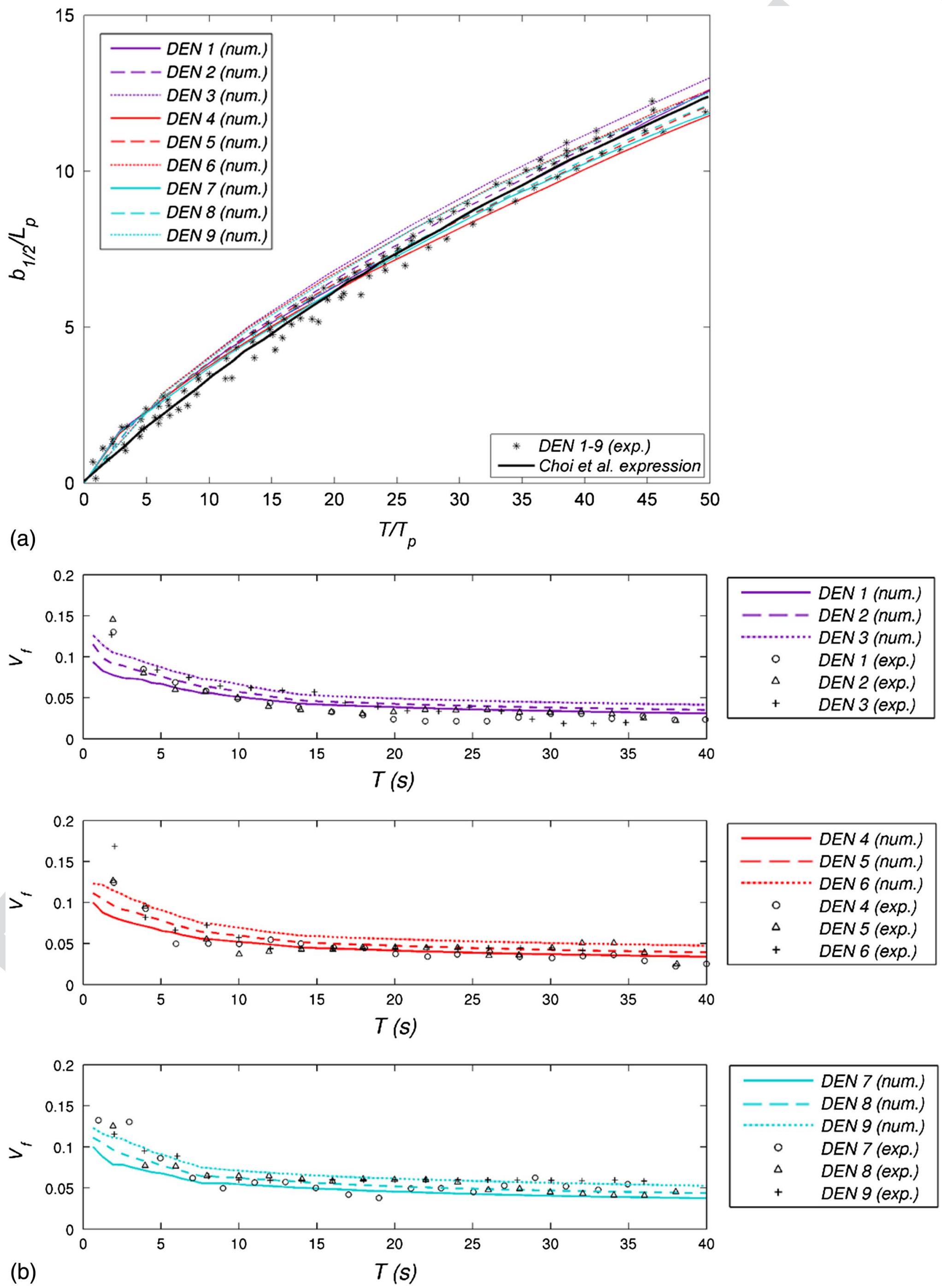

Fig. 13. Comparison between the numerical and experimental results of Choi and Garcia (2001): (a) dimensionless maximum half-width versus time; and (b) velocity front.

generates the best results. We recognize that applying the κ-ε turbulence model, which solves two more equations, is demanding in terms of computation time. Both the mixing length model and the constant model can generate good approximations within a more reasonable timeframe for field applications.

The results obtained through this study show that by applying the previous guidelines, 3D hydrodynamic models can reproduce density current flows in stagnant receiving waters with errors of less than 1.3% for a minimum dilution line and of 6% for a maximum velocity line. Due to the previous guidelines having been obtained from validations based on measurements taken under environmental controlled conditions, this contribution represents a first step toward the validation of such 3D hydrodynamic models for solving current flows under real environmental conditions. Accordingly, a next step would involve checking and validating the previous guidelines in field-scale applications where bathymetry and environmental conditions can have a significant influence on the density current evolution. Note that these models have been widely validated in terms of the reproduction of main coastal dynamics either independently or through robust coupling with other models (e.g., atmospheric and wave models).

Acknowledgments

This study was partially funded by the Ministry of Economy and Competitiveness (MINECO) under research project TRA2011-28900 (PLVMA3D). B. Pérez-Díaz would like to thank MINECO for providing funding under the FPI Program (research fellowship, reference number BES-2012-053693) and the Coasts and Ocean Group of HR Wallingford for their assistance with numerical tasks.

References

Aidun, C. K., and J. R. Clausen. 2010. "Lattice-Boltzmann method for complex flows." *Annu. Rev. Fluid Mech.* 42 (1): 439–472. https://doi.org/10.1146/annurev-fluid-121108-145519.

Akiyama, J., and H. Stefan. 1985. "Turbidity current with erosion and deposition." *J. Hydraul. Eng.* 111 (12): 1473–1496. https://doi.org/10.1061/(ASCE)0733-9429(1985)111:12(1473).

Alavian, V. 1986. "Behavior of density currents on an incline." *J. Hydraul. Eng.* 112 (1): 27–42. https://doi.org/10.1061/(ASCE)0733-9429(1986)112:1(27).

Almgren, A. S., J. B. Bell, and W. G. Szymczak. 1996. "A numerical method for the incompressible Navier-Stokes equations based on an approximate projection." *SIAM J. Sci. Comput.* 17 (2): 358–369. https://doi.org/10.1137/S1064827593244213.

Birman, V., J. Margin, and E. Meigurg. 2005. "The non-Boussinesq lock-exchange problem. Part 2: High-resolution simulations." *J. Fluid Mech.* 537: 125–144. https://doi.org/10.1017/S0022112005005033.

Bombardelli, F. A., and M. H. Garca. 2002. Three-dimensional hydrodynamic modeling of density current in the Chicago river, Illinois. Rep. No. HES 68.

Bourban, S. E. 2013. "Stratified shallow flow modelling." Ph.D. thesis, Open Univ.

Bournet, P. E., D. Dartus, B. Tassin, and B. Vinçon-Leite. 1999. "Numerical investigation of plunging density current." *J. Hydraul. Eng.* 125 (6): 584–594. https://doi.org/10.1061/(ASCE)0733-9429(1999)125:6(584).

Bradford, S. F., N. D. Katopodes, and G. Parker. 1997. "Characteristic of turbid underflows." *J. Hydraul. Eng.* 123 (5): 420–431. https://doi.org/10.1061/(ASCE)0733-9429(1997)123:5(420).

Brørs, B. R., and K. J. Eidsvik. 1992. "Dynamic Reynolds stress modeling of turbidity currents." *J. Geophys. Res.* 97 (C6): 9645. https://doi.org/10.1029/92JC00587.

Cantero, M. I., S. Balachandar, and M. H. Garcia. 2007. "High-resolution simulations of cylindrical density currents." *J. Fluid Mech.* 590 (3): 437–469.

Cantero, M. I., S. Balachandar, M. H. Garcia, and J. P. Ferry. 2006. "Direct numerical simulations of planar and cylindrical density currents." *J. Appl. Mech.* 73 (6): 923. https://doi.org/10.1115/1.2173671.

Choi, S. U. 1999. "Layer-averaged modeling of two-dimensional turbidity currents with a dissipative-Galerkin finite element method. Part II: Sensitivity analysis and experimental verification." *J. Hydraul. Res.* 37 (2): 257–271. https://doi.org/10.1080/00221689909498310.

Choi, S. U., and M. H. Garcia. 1995. "Modeling of one-dimensional turbidity currents with a dissipative-Galerkin finite element method." *J. Hydraul. Res.* 33 (5): 623–648. https://doi.org/10.1080/00221689509498561.

Choi, S. U., and M. H. Garcia. 2001. "Spreading of gravity plumes on an incline." *Coastal Eng. J.* 43 (04): 221–237. https://doi.org/10.1142/S0578563401000359.

Choi, S. U., and M. H. Garcia. 2002. "k-ε turbulence modeling of density currents developing two dimensionally on a slope." *J. Hydraul. Eng.* 128 (1): 55–63. https://doi.org/10.1061/(ASCE)0733-9429(2002)128:1(55).

Chu, V. H., and G. H. Jirka. 1987. "Surface buoyant jets and plumes." In *Encyclopedia of fluid mechanics*.

Dallimore, C. J., J. Imberger, and T. Ishikawa. 2001. "Entrainment and turbulence in saline underflow in Lake Ogawara." *J. Hydraul. Eng.* 127 (11): 937–948. https://doi.org/10.1061/(ASCE)0733-9429(2001)127:11(937).

Dawoud, M. A., and M. M. Al Mulla. 2012. "Environmental impacts of seawater desalination: Arabian gulf case study." *Int. J. Environ. Sustainability* 1 (3): 22–37. https://doi.org/10.24102/ijes.v1i3.96.

Eidsvik, K. J., and B. R. Brørs. 1989. "Self-accelerated turbidity current prediction based upon (k-ε) turbulence." *Cont. Shelf Res.* 9 (7): 617–627. https://doi.org/10.1016/0278-4343(89)90033-2.

Ellison, T. H., and J. S. Turner. 1959. "Turbulent entrainment in stratified flows." *J. Fluid Mech.* 6 (3): 423. https://doi.org/10.1017/S0022112059000738.

Farrell, G. J., and H. G. Stefan. 1988. "Mathematical modeling of plunging reservoir flows." *J. Hydraul. Res.* 26 (5): 525–537. https://doi.org/10.1080/00221688809499191.

Fernandez, R. L., and J. Imberger. 2006. "Bed roughness induced entrainment in a high Richardson number underflow." *J. Hydraul. Res.* 44 (6): 725–738. https://doi.org/10.1080/00221686.2006.9521724.

Firoozabadi, B., H. Afshin, and E. Aram. 2009. "Three-dimensional modeling of density current in a straight channel." *J. Hydraul. Eng.* 135 (5): 393–402. https://doi.org/10.1061/(ASCE)HY.1943-7900.0000026.

Garcia, M. H. 1993. "Hydraulic jumps in sediment driven bottom currents." *J. Hydraul. Eng.* 119 (10): 1094–1117.

Gerber, G., G. Diedericks, and G. R. Basson. 2011. "Particle image velocimetry measurements and numerical modeling of a saline density current." *J. Hydraul. Eng.* 137 (3): 333–342. https://doi.org/10.1061/(ASCE)HY.1943-7900.0000304.

Gray, T. E., J. Alexander, and M. R. Leeder. 2006. "Longitudinal flow evolution and turbulence structure of dynamically similar, sustained, saline density and turbidity currents." *J. Geophys. Res.* 111 (C8): C08015. https://doi.org/10.1029/2005JC003089.

Härtel, C., E. Meiburg, and F. Necker. 2000. "Analysis and direct numerical simulation of the flow at a gravity-current head. Part 1: Flow topology and front speed for slip and no-slip boundaries." *J. Fluid Mech.* 418: 189–212. https://doi.org/10.1017/S0022112000001221.

Hebbert, B., J. Patterson, I. Loh, and J. Imberger. 1979. "Collie river underflow into the Wellington reservoir." *J. Hydraul. Div.* 105 (5): 533–545.

Heller, V. 2011. "Scale effects in physical hydraulic engineering models." *J. Hydraul. Res.* 49 (3): 293–306.

Hervouet, J.-M. 2007. *Hydrodynamics of free surface flows: Modelling with the finite element method*. Hoboken, NJ: Wiley.

Hodges, B. R., J. E. Furnans, and P. S. Kulis. 2011. "Thin-layer gravity current with implications for desalination brine disposal." *J. Hydraul. Eng.* 137 (3): 356–371. https://doi.org/10.1061/(ASCE)HY.1943-7900.0000310.

Hossain, M. S., and W. Rodi. 1982. *Turbulent buoyant jets and plumes*. New York: Pergamon Press.

Huppert, H. E. 2006. "Gravity currents: A personal perspective." *J. Fluid Mech.* 554: 299–322. https://doi.org/10.1017/S002211200600930X.

Imran, J., G. Parker, and N. Katopodes. 1998. “A numerical model of channel inception on submarine fans.” *J. Geophys. Res. Oceans* 103 (C1): 1219–1238. https://doi.org/10.1029/97JC01721.

Islam, M. A., and J. Imran. 2010. “Vertical structure of continuous release saline and turbidity currents.” *J. Geophys. Res.* 115 (C8): C08025. https://doi.org/10.1029/2009JC005365.

Kulis, P., and B. R. Hodges. 2006. “Modeling gravity currents in shallow bays using a sigma coordinate model.” In *Proc., 7th Int. Conf. on Hydroscience and Engineering*. Philadelphia.

Kurganov, A., and G. Petrova. 2007. “A second-order well-balanced positivity preserving central-upwind scheme for the Saint-Venant system. 5 (1): 133–160.

La Rocca, M., C. Adduce, G. Sciortino, and A. B. Pinzon. 2008. “Experimental and numerical simulation of three-dimensional gravity currents on smooth and rough bottom.” *Phys. Fluids* 20 (10): 106603. https://doi.org/10.1063/1.3002381.

La Rocca, M., C. Adduce, G. Sciortino, A. B. Pinzon, and M. A. Boniforti. 2012. “A two-layer, shallow-water model for 3D gravity currents.” *J. Hydraul. Res.* 50 (2): 208–217. https://doi.org/10.1080/00221686.2012.667680.

La Rocca, M., and A. B. Pinzon. 2010. “Experimental and theoretical modelling of 3D gravity currents.” In *Numerical simulations: Examples and applications in computational fluid dynamics*.

Laspidou, C., K. Hadjibiros, and S. Gialis. 2010. “Minimizing the environmental impact of sea brine disposal by coupling desalination plants with solar saltworks: A case study for Greece.” *Water* 2 (1): 75–84. https://doi.org/10.3390/w2010075.

Lattemann, S., and T. Höpner. 2008. “Environmental impact and impact assessment of seawater desalination.” *Desalination* 220 (1): 1–15. https://doi.org/10.1016/j.desal.2007.03.009.

Launder, B. E., A. Morse, W. Rodi, and D. B. Spalding. 1973. “Prediction of free shear flows: A comparison of the performance of six turbulence models.” In *Proc., NASA Conf. on Free Turbulent Shear Flows*.

Launder, B. E., and D. B. Spalding. 1974. “The numerical computation of turbulent flows.” *Comput. Methods Appl. Mech. Eng.* 269–289. https://doi.org/10.1016/0045-7825(74)90029-2.

LNHE (National Hydraulic and Environment Laboratory). 2007. *Telemac modelling system: Telemac-3D code, operating manual*. LNHE.

Lombardi, V., C. Adduce, and M. La Rocca. 2018. “Unconfined lock-exchange gravity currents with variable lock width: Laboratory experiments and shallow-water simulations.” *J. Hydraul. Res.* 56 (3): 399–411. https://doi.org/10.1080/00221686.2017.1372817.

Lombardi, V., C. Adduce, G. Sciortino, and M. La Rocca. 2015. “Gravity currents flowing upslope: Laboratory experiments and shallow-water simulations.” *Phys. Fluids* 27 (1): 016602. https://doi.org/10.1063/1.4905305.

Lowe, R. J., J. W. Rottman, and P. F. Linden. 2005. “The non-Boussinesq lock-exchange problem. Part 1: Theory and experiments.” *J. Fluid Mech.* 537: 101–124. https://doi.org/10.1017/S0022112005005069.

Madsen, P., M. Rugbjerg, and I. Warren. 1988. “Subgrid modelling in depth intergrated flows.” In *Proc., 21st Coastal Engineering Conf.*, 505–5011. New York: ASCE.

Mahgoub, M., R. Hinkelmann, and M. L. Rocca. 2015. “Three-dimensional non-hydrostatic simulation of gravity currents using TELEMAC3D and comparison of results to experimental data.” *Progress Comput. Fluid Dyn. Int. J.* 15 (1): 56. https://doi.org/10.1504/PCFD.2015.067325.

Munk, W., and E. Anderson. 1948. “Notes on a theory of the thermocline.” *J. Mar. Res.* 3: 276–295.

Nezu, I., and H. Nakagawa. 1993. *Turbulence in open channel flows*. IAHR monograph series. Rotterdam, Netherlands: A.A. Balkema.

Ottolenghi, L., C. Adduce, R. Inghilesi, V. Armenio, and F. Roman. 2016a. “Entrainment and mixing in unsteady gravity currents.” *J. Hydraul. Res.* 54 (5): 541–557. https://doi.org/10.1080/00221686.2016.1174961.

Ottolenghi, L., C. Adduce, R. Inghilesi, F. Roman, and V. Armenio. 2016b. “Mixing in lock-release gravity currents propagating up a slope.” *Phys. Fluids* 28 (5): 056604. https://doi.org/10.1063/1.4948760.

Ottolenghi, L., C. Adduce, F. Roman, and V. Armenio. 2017a. “Analysis of the flow in gravity currents propagating up a slope.” *Ocean Modell.* 115: 1–13. https://doi.org/10.1016/j.ocemod.2017.05.001.

Ottolenghi, L., C. Cenedese, and C. Adduce. 2017b. “Entrainment in a dense current flowing down a rough sloping bottom in a rotating fluid.” *J. Phys. Oceanogr.* 47 (3): 485–498. https://doi.org/10.1175/JPO-D-16-0175.1.

Ottolenghi, L., P. Prestininzi, A. Montessori, C. Adduce, and M. La Rocca. 2018. “Lattice Boltzmann simulations of gravity currents.” *Eur. J. Mech. B. Fluids* 67: 125–136. https://doi.org/10.1016/j.euromechflu.2017.09.003.

Palomar, P. 2014. “Experimental and numerical optimization of brine discharges in the marine environment.” Ph.D. thesis, Universidad de Cantabria.

Papakonstantis, I. G., and G. C. Christodoulou. 2010. “Spreading of round dense jets impinging on a horizontal bottom.” *J. Hydro-environ. Res.* 4 (4): 289–300. https://doi.org/10.1016/j.jher.2010.07.001.

Parker, G., Y. Fukushima, and H. M. Pantin. 1986. “Self-accelerating turbidity currents.” *J. Fluid Mech.* 171: 145–181. https://doi.org/10.1017/S0022112086001404.

Parker, G., M. Garcia, Y. Fukushima, and W. Yu. 1987. “Experiments on turbidity currents over an erodible bed.” *J. Hydraul. Res.* 25 (1): 123–147. https://doi.org/10.1080/00221688709499292.

Patterson, M. D., J. E. Simpson, S. B. Dalziel, and N. Nikiforakis. 2005. “Numerical modelling of two-dimensional and axisymmetric gravity currents.” *Int. J. Numer. Methods Fluids* 47 (10–11): 1221–1227. https://doi.org/10.1002/fld.841.

Patterson, M. D., J. E. Simpson, S. B. Dalziel, and G. J. F. van Heijst. 2006. “Vortical motion in the head of an axisymmetric gravity current.” *Phys. Fluids* 18 (4): 046601. https://doi.org/10.1063/1.2174717.

Pérez-Díaz, B., P. Palomar, and S. Castanedo. 2016. “PIV-PLIF characterization of density currents.” In *Proc., 4th IAHR Europe Congress*, 174–178. Liege, Belgium.

Pérez-Díaz, B., P. Palomar, S. Castanedo, and A. Álvarez. 2018. “PIV-PLIF characterization of nonconfined saline density currents under different flow conditions.” *J. Hydraul. Eng.* 144 (9): 04018063. https://doi.org/10.1061/(ASCE)HY.1943-7900.0001511.

Prestininzi, P., V. Lombardi, and M. L. Rocca. 2016. “Curved boundaries in multi-layer shallow water lattice Boltzmann methods: Bounce back versus immersed boundary.” *J. Comput. Sci.* 16: 16–28. https://doi.org/10.1016/j.jocs.2016.03.001.

Rocca, M. L., C. Adduce, V. Lombardi, G. Sciortino, and R. Hinkelmann. 2012. “Development of a lattice Boltzmann method for two-layered shallow-water flow.” *Int. J. Numer. Methods Fluids* 70 (8): 1048–1072. https://doi.org/10.1002/fld.2742.

Rodi, W. 1972. “The prediction of free turbulent boundary layers by use of a two-equation model of turbulence.” Ph.D. thesis, Imperial College London, Univ. of London.

Rodi, W. 1975. “A note on the empirical constant in the Kolmogorov-Prandtl eddy-viscosity expression.” *J. Fluids Eng.* 97 (3): 386. https://doi.org/10.1115/1.3447325.

Rodi, W. 1984. Turbulence models and their application in hydraulics: A state of the art review. Rep. No. Delft, Netherlands: International Association for Hydraulic Research (Section on Hydraulics Instrumentation).

Rodi, W. 1987. “Examples of calculation methods for flow and mixing in stratified fluids.” *J. Geophys. Res.* 92 (C5): 5305. https://doi.org/10.1029/JC092iC05p05305.

Sánchez-Lizaso, J. L., J. Romero, J. Ruiz, E. Gacia, J. L. Buceta, O. Invers, Y. Fernández Torquemada, J. Mas, A. Ruiz-Mateo, and M. Manzanera. 2008. “Salinity tolerance of the Mediterranean seagrass *Posidonia oceanica*: Recommendations to minimize the impact of brine discharges from desalination plants.” *Desalination* 221 (1): 602–607. https://doi.org/10.1016/j.desal.2007.01.119.

Sciortino, G., C. Adduce, and V. Lombardi. 2018. “A new front condition for non-Boussinesq gravity currents.” *J. Hydraul. Res.* 1–9.

Shao, D., A. W. Law, and H. Li. 2008. “Brine discharges into shallow coastal waters with mean and oscillatory tidal currents.” *J. Hydro-environ. Res.* 2 (2): 91–97. https://doi.org/10.1016/j.jher.2008.08.001.

Simpson, J. E. 1997. *Gravity currents: The environment and the laboratory*. New York: Cambridge University Press.

Smagorinsky, J. 1963. "General circulation experiments with the primitive equations." *Mon. Weather Rev.* 91 (3): 99–164. https://doi.org/10.1175/1520-0493(1963)091<0099:GCEWTP>2.3.CO;2.

Stacey, M. W., and A. J. Bowen. 1988a. "The vertical structure of density and turbidity currents: Theory and observations." *J. Geophys. Res.* 93 (C4): 3528. https://doi.org/10.1029/JC093iC04p03528.

Stacey, M. W., and A. J. Bowen. 1988b. "The vertical structure of turbidity currents and a necessary condition for self-maintenance." *J. Geophys. Res.* 93 (C4): 3543. https://doi.org/10.1029/JC093iC04p03543.

Ungarish, M. 2007a. "Axisymmetric gravity currents at high Reynolds number: On the quality of shallow-water modeling of experimental observations." *Phys. Fluids* 19 (3): 036602. https://doi.org/10.1063/1.2714990.

Ungarish, M. 2007b. "A shallow-water model for high-Reynolds-number gravity currents for a wide range of density differences and fractional depths." *J. Fluid Mech.* 579: 373. https://doi.org/10.1017/S0022112007005484.

Ungarish, M. 2008. "Energy balances and front speed conditions of two-layer models for gravity currents produced by lock release." *Acta Mech.* 201 (1–4): 63–81. https://doi.org/10.1007/s00707-008-0073-z.

Viollet, P. L. 1988. "On the numerical modelling of stratified flows." In *Physical processes in estuaries*, 257–277. Berlin: Springer.

Queries

1. Please provide the ASCE Membership Grades for the authors who are members.

2. Please provide author titles (e.g., Professor, Director) for all affiliation footnotes.

3. Please provide street address for the author "P. Palomar".

4. Please check the hierarchy of section heading levels.

5. [ASCE Open Access: Authors may choose to publish their papers through ASCE Open Access, making the paper freely available to all readers via the ASCE Library website. ASCE Open Access papers will be published under the Creative Commons-Attribution Only (CC-BY) License. The fee for this service is $1750, and must be paid prior to publication. If you indicate Yes, you will receive a follow-up message with payment instructions. If you indicate No, your paper will be published in the typical subscribed-access section of the Journal.]

6. ASCE style does not allow for sections with only one sentence. As such, the sentence below "Methods" has been deleted. Please confirm no errors were introduced.

7. ASCE asks that there be at least two subheadings under a given heading. As such, the heading "Initial Model Setup" has been changed to a Level 2 heading. Please confirm the headings as shown.

8. ASCE style requires that all fractions presented within paragraphs of text should be presented in a slashed down form (and not in stacked form). Please check all instances in the article which are slashed down forms of the inline fractions.

9. ASCE asks that Reynolds number be a "R" in Helvetica font, and Froude number be a "F" in Helvetica font. As such, these variables have been changed throughout the manuscript. Please confirm no errors have been introduced.

10. Please confirm that the "F' in variable "Sc_F" refers to Froude number.

11. The term "Hydrostatic-hyp." was changed to "Hydrostatic hypothesis". Please confirm this is correct

12. Please confirm Table 5 is correct as shown.

13. Headings in Table 3 have been changed to non-bold font. Please confirm this is correct and no errors were introduced.

14. Please confirm that the variables for normalized maximum velocity and minimum dilution are correct (i.e., should "max" and "min" be subscript?).

15. To comply with ASCE style the term "*Q* & *V*" was changed to "*Q* and *V*" throughout. Please confirm no errors were introduced.

16. Please confirm Table 5 is correct as shown.

17. Bold values in the Table 5 headings have been changed to non-bold font. Please confirm no errors were introduced.

18. Please provide issue number for Birman et al. (2005).

19. Please provide publisher name and location for Bombardelli and Garca (2002).

20. Please provide department name for Bourban (2013).

21. This query was generated by an automatic reference checking system. This reference could not be located in the databases used by the system. While the reference may be correct, we ask that you check it so we can provide as many links to the referenced articles as possible.

22. Please provide publisher name and location for Chu and Jirka (1987).

23. This query was generated by an automatic reference checking system. This reference could not be located in the databases used by the system. While the reference may be correct, we ask that you check it so we can provide as many links to the referenced articles as possible.

24. Please provide issue number for Härtel et al. (2000).

25. This query was generated by an automatic reference checking system. This reference could not be located in the databases used by the system. While the reference may be correct, we ask that you check it so we can provide as many links to the referenced articles as possible.

26. This query was generated by an automatic reference checking system. This reference could not be located in the databases used by the system. While the reference may be correct, we ask that you check it so we can provide as many links to the referenced articles as possible.

27. Please provide issue number for Huppert (2006).

28. Please provide the publisher or sponsor name and location (not the conference location) for Kulis and Hodges (2006).

29. This query was generated by an automatic reference checking system. This reference could not be located in the databases used by the system. While the reference may be correct, we ask that you check it so we can provide as many links to the referenced articles as possible.

30. Please provide publisher name and location for La Rocca and Pinzon (2010).

31. Please provide the publisher or sponsor name and location (not the conference location) for Launder et al. (1973).

32. Please provide volume number and issue number for Launder et al. (2017).

33. Please provide publisher location for LNHE (2007).

34. Please provide issue number for Lowe et al. (2005).

35. Please provide issue number for Munk and Anderson (1948).

36. This query was generated by an automatic reference checking system. This reference could not be located in the databases used by the system. While the reference may be correct, we ask that you check it so we can provide as many links to the referenced articles as possible.

37. Please provide issue number for Ottolenghi et al. (2017a).

38. Please provide issue number for Ottolenghi et al. (2018).

39. Please provide depatment name for Palomar (2014).

40. Please provide issue number for Parker et al. (1986).

41. Please provide the publisher or sponsor name and location (not the conference location) for Pérez-Daz et al. (2016).

42. Please provide volume number and issue number for Sciortino et al. (2018).

43. This query was generated by an automatic reference checking system. This reference could not be located in the databases used by the system. While the reference may be correct, we ask that you check it so we can provide as many links to the referenced articles as possible.

44. Please provide issue number for Ungarish (2007b).